Journal of Electromagnetic Waves and Applications

ISSN: 0920-5071 (Print) 1569-3937 (Online) Journal homepage: http://www.tandfonline.com/loi/tewa20

Efficient Evaluation of Sommerfeld Integrals for Tm Wave Scattering By Buried Objects

T.J. Cui & W.C. Chew

To cite this article: T.J. Cui & W.C. Chew (1998) Efficient Evaluation of Sommerfeld Integrals for Tm Wave Scattering By Buried Objects, Journal of Electromagnetic Waves and Applications, 12:5, 607-657, DOI: 10.1163/156939398X00160

To link to this article: http://dx.doi.org/10.1163/156939398X00160

Published online: 03 Apr 2012.

Journal of Electromagnetic Waves and Applications, Vol. 12, 607–657, 1998

EFFICIENT EVALUATION OF SOMMERFELD INTEGRALS FOR TM WAVE SCATTERING BY BURIED OBJECTS

T. J. Cui and W. C. Chew

Center for Computational Electromagnetics
Department of Electrical and Computer Engineering
University of Illinois at Urbana-Champaign
Urbana, IL 61801-2991

Abstract–Unlike the scattering problem in homogeneous space, intensive computations of Sommerfeld integrals are involved in the EM scattering of buried scatterers. There are mainly three bottlenecks of the CPU time for such problem: matrix filling, matrix inversion and calculation of the scattered fields. For moderately sized problems, extensive numerical experience shows that the CPU time used in the first and third items (concerned with the Sommerfeld integrals) is much more than that used in the matrix inversion. Therefore an efficient method for solving such buried object problems requires the fast evaluation of such Sommerfeld integrals. In this paper, several efficient methods are presented to evaluate the integrals that appear in the TM wave scattering by two-dimensional buried dielectric and conducting cylinders. In the numerical integration method, the original integrating path is deformed to the steepest-descent paths to expedite the numerical integration and yield a more stable computation result. In the method of steepest descent, the leading and higher-order approximation of the saddle point, and the contribution of the branch point are formulated. However these formulations are invalid near the so called "critical angles". In the uniform asymptotic expansion method, we improve the approximations near such critical angles to yield satisfactory results. Finally, numerous numerical examples are given by using the fast evaluation methods. Numerical results show that the leading-order approximation and the uniform asymptotic solution can expedite the buried object scattering problem, and the CPU time will be reduced several thousands times.

1. INTRODUCTION

Electromagnetic scattering has been a topic of significant interest for several decades, and the associated research methods have been investigated by numerous authors [1–10]. These methods were originally developed for scatterers residing in a homogeneous space, most of which reduce the original problem to a matrix equation. In such methods, the main bottleneck of the computation comes from the matrix inversion, which is intensive when the electrical dimensions of the scatterers become large. To expedite the solution time, much effort has been invested in "fast solution methods", for example, the fast multipole method (FMM), multilevel algorithms, wavelet expansion, fast steepest descent path algorithm, etc. [11–20].

Besides EM scattering in homogeneous space, scattering by scatterers buried underground or under water is also of great importance, and finds wide applications in the detection of buried pipes, cables, and other mineral deposits. Generally speaking, the research methods used in the homogeneous space case can also be utilized in the buried problem, for example, the method of moments (MOM), the finite-element method (FEM), etc. [21–30]. Compared to the homogeneous space case, there is a severe problem in the scattering computations of buried scatterers: that is the computation time is often more than hundreds of times longer. Therefore, it is very difficult to handle large-scale buried scatterers by using the current methods [21–30], even though these scatterers are of great interest in some applications, such as the detection of submarines.

Unlike scattering problems in homogeneous space, intensive computations of Sommerfeld integrals are involved in the EM scattering computation of buried scatterers. Therefore, there are three main bottlenecks of the computation for such a problem: matrix filling, matrix inversion, and calculation of the scattered fields. As an illustration, we consider a two-dimensional case with TM wave incidence. Suppose that the buried scatterers are divided into N cells and the scattered fields are computed at M points. Then there will be N^2 Sommerfeld integrals in the matrix filling, and $M \times N$ Sommerfeld integrals in the calculation of scattered fields. In the matrix inversion, however, there are only $O(N^3)$ algebraic operations for Gaussian elimination method. But each Sommerfeld integral takes many computations to evaluate. That is to say, the CPU time used in matrix filling and calculation of scattered fields, which involve the computation of integrals, is much more than that used in the matrix inversion for moderately sized problem. Therefore the essence of the efficient method for buried problems is the fast evaluation of such Sommerfeld integrals.

In this paper, several fast methods are presented to evaluate integrals

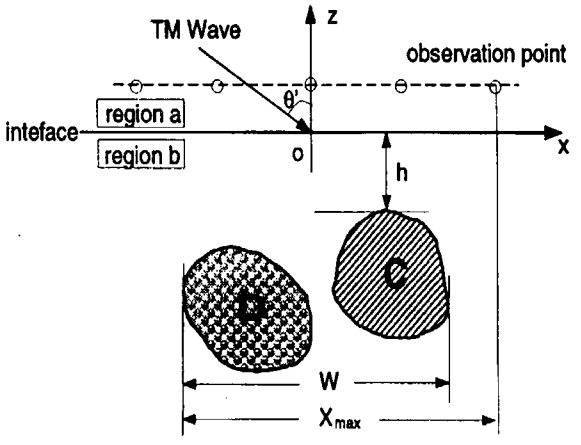

Figure 1. Dielectric cylinders and conducting cylinders buried under a half space.

that appear in the TM wave scattering by two-dimensional buried dielectric and conducting cylinders. After a brief description of the modeling for such problem, a numerical integration method is introduced in Section 3 where the original integration path is deformed to the steepest-descent path to expedite the numerical integration and to yield a more stable computation result. In Section 4, the method of steepest descent is used to evaluate the integrals. Here the leading and higher order approximation of the saddle point, and the contribution of the branch point are formulated. However these formulations are invalid near a so called "critical angles". In Section 5, the uniform asymptotic expansion method is used to improve the approximations near the critical angles. Finally, numerous numerical examples are given by using these efficient methods. Numerical results show that the leading-order approximation and the uniform asymptotic solution can expedite the buried scattering problem, and the CPU time will be reduced thousands of times.

2. SIMPLE DESCRIPTION OF THE MODELING

We consider multiple dielectric cylinders and conducting cylinders buried under a half space, as shown in Fig. 1. We denote the collection of the dielectric cylinders as $\mathbf{D}$ with relative permittivity $\epsilon_r(x, z)$, and the collection of the conducting cylinders as $\mathbf{C}$. The half space is represented by

relative permittivities ϵ_a and ϵ_b. A plane-polarized electromagnetic wave with wave number k and electric field perpendicular to the x-z plane (TM wave) is incident from the upper space at an oblique angle θ', as illustrated in Fig. 1. Here, h is the minimum buried height of the scatterers; W is the maximum width of the scatterers; X_{max} is the longest distance in x coordinate from the fixed observation point (x, z) to the scatterers. Throughout this paper the time dependence of $e^{-i\omega t}$ is assumed and suppressed.

From EM theory [30, 31, 33], electric fields excited by the electric current J_D inside the dielectric cylinders and J_C on the surfaces of the conducting cylinders can be formulated. In the lower half space,

$$\begin{aligned} E_{bz}(x,z) = &-\frac{\omega\mu_0}{4\pi}\int_{\mathbf{D}} J_D(x',z')\int_{-\infty}^{+\infty}\beta_b^{-1} \\ &\times\left[e^{i\beta_b|z-z'|}+Re^{-i\beta_b(z+z')}\right]e^{i\xi(x-x')}d\xi dx'dz' \\ &-\frac{\omega\mu_0}{4\pi}\int_{\mathbf{C}} J_C(x',z')\int_{-\infty}^{+\infty}\beta_b^{-1} \\ &\times\left[e^{i\beta_b|z-z'|}+Re^{-i\beta_b(z+z')}\right]e^{i\xi(x-x')}d\xi dc'; \end{aligned} \tag{1}$$

in the upper half space,

$$\begin{aligned} E_{az}(x,z) = &-\frac{\omega\mu_0}{4\pi}\int_{\mathbf{D}} J_D(x',z')\int_{-\infty}^{+\infty}\beta_b^{-1}\times Te^{i(\beta_a z-\beta_b z')}e^{i\xi(x-x')}d\xi dx'dz' \\ &-\frac{\omega\mu_0}{4\pi}\int_{\mathbf{C}} J_C(x',z')\int_{-\infty}^{+\infty}\beta_b^{-1}\times Te^{i(\beta_a z-\beta_b z')}e^{i\xi(x-x')}d\xi dc'. \end{aligned} \tag{2}$$

Here

$$\beta_a = \sqrt{k_a^2-\xi^2}, \qquad \beta_b = \sqrt{k_b^2-\xi^2} \tag{3}$$

with $k_a = k\sqrt{\epsilon_a}$ and $k_b = k\sqrt{\epsilon_b}$ being wave numbers in spaces a and b. And,

$$R = \frac{\beta_b-\beta_a}{\beta_b+\beta_a}, \qquad T = 1+R \tag{4}$$

are the reflection and transmission coefficients of the half space.

Using the boundary conditions, (1) can be easily changed to an integral equation which has to be solved by numerical methods, for example, the method of moments. If the dielectric cylinder $\mathbf{D}$ is split into M square

cells and the conducting cylinder **C** into $N-M$ line segments, the integral equation will reduce to a matrix equation [30]

$$\mathbf{A}\cdot\mathbf{u}=\mathbf{E}_{\mathrm{b}}^{\mathrm{i}} \tag{5}$$

where $\mathbf{u}=[E_1,\ldots,E_M,J_{M+1},\ldots,J_N]^T$, $\mathbf{E}_{\mathrm{b}}^{\mathrm{i}}=[E_{b1}^i,\ldots,E_{bN}^i]$. Here, E_{bm} is the total electric field inside the dielectric cylinder ($m=1,\ldots,M$), J_n is the electric current around the conducting cylinder ($n=M+1,\ldots,N$), and E_{bm}^i is the incident electric field in region b ($m=1,\ldots,N$). The matrix **A** is given by

$$A_{mm}=\begin{cases}\dfrac{\epsilon_{rm}}{\epsilon_b}-i\dfrac{\pi}{2}\left(\dfrac{\epsilon_{rm}}{\epsilon_b}-1\right)k_ba_mH_1^{(1)}(k_ba_m)\\ \qquad -i\dfrac{k^2}{4\pi}(\epsilon_{rm}-\epsilon_b)S_mI(m,m), & 1\le m\le M,\\ \dfrac{\eta_0}{4}kc_m\left[1-\dfrac{(k_bc_m)^2}{48}+i\dfrac{2}{\pi}\left(\ln\dfrac{k_bc_m}{4}-1\right)\right.\\ \qquad \left.+\dfrac{1}{\pi}I(m,m)\right], & M+1\le m\le N;\end{cases} \tag{6}$$

$$A_{mn}=\begin{cases}-i\dfrac{k^2}{4}(\epsilon_{rn}-\epsilon_b)S_n\left[H_0^{(1)}(k_b\rho_{mn})+\dfrac{1}{\pi}I(m,n)\right], & 1\le n\le M,\\ \dfrac{\eta_0}{4}kc_n\left[H_0^{(1)}(k_b\rho_{mn})+\dfrac{1}{\pi}I(m,n)\right], & M+1\le n\le N.\end{cases} \quad (n\neq m) \tag{7}$$

in which (x_n,z_n) are the coordinates of cell n, S_n and a_n are the area and equivalent radius of the square cell, c_n is the length of the line cell, $\rho_{mn}=\sqrt{(x_m-x_n)^2+(z_m-z_n)^2}$ is the distance between cells m and n. Finally, $I(m,n)$ is a Sommerfeld integral defined as

$$I(m,n)=\int_{-\infty}^{+\infty}\beta_b^{-1}Re^{-i\beta_b(z_m+z_n)}e^{i\xi(x_m-x_n)}d\xi. \tag{8}$$

In the upper half space, the scattered electric field from the buried scatterers can be formulated from (2)

$$E_a^s(x,z)=i\frac{k^2}{4\pi}\sum_{n=1}^{M}(\epsilon_{rn}-\epsilon_b)E_nS_nK_n(x,z)-\frac{\eta_0}{4\pi}\times\sum_{n=M+1}^{N}J_nkc_nK_n(x,z) \tag{9}$$

where $K_n(x,z)$ is the Sommerfeld integral

$$K_n(x,z) = \int_{-\infty}^{+\infty} \beta_b^{-1} T e^{i(\beta_a z - \beta_b z_n)} e^{i\xi(x-x_n)} d\xi. \tag{10}$$

From the above procedure, there are N^2 Sommerfeld integrals $I(m,n)$ in the matrix filling, and $M \times N$ integrals $K_n(x,z)$ in the computation of the scattered fields, that are CPU time intensive. So it is necessary to investigate fast methods for computations of these integrals.

3. NUMERICAL INTEGRATION ALONG THE STEEPEST-DESCENT PATHS

The first efficient method to treat the integrals $I(m,n)$ and $K_n(x,z)$ is by numerical integration along the steepest-descent paths, instead of the original path — the real ξ-axis.

3.1 Integral $I(m,n)$

From (8), there are three critical points in the integral $I(m,n)$. They are the saddle point ξ_0, the branch points k_a and k_b. We let

$$\Lambda h_1(\xi) = -i\beta_b(z_m + z_n) \pm i\xi(x_m - x_n) \tag{11}$$

in which Λ is a large parameter. We choose $\pm$ in (11) to ensure that the saddle point ξ_0 is located in the positive ξ-axis because both "+" and "$-$" are correct in (8) due to symmetry. From $h_1'(\xi_0) = 0$, we get the saddle point

$$\xi_0 = k_b \sin\theta_0, \qquad \theta_0 = \tan^{-1}\left|\frac{x_m - x_n}{z_m + z_n}\right| \tag{12}$$

in which $z_m, z_n < 0$, as shown in Fig. 1.

To define the steepest-descent path passing through the saddle point, we introduce a change of variable [31]

$$-s^2 = h_1(\xi) - h_1(\xi_0). \tag{13}$$

Substituting (11) and (12) into (13) yields

$$i\frac{\Lambda s^2}{\bar{\rho}_{mn}} = \sqrt{k_b^2 - \xi^2}\cos\theta_0 + \xi\sin\theta_0 - k_b, \tag{14}$$

where $\bar{\rho}_{mn} = \sqrt{(x_m - x_n)^2 + (z_m + z_n)^2}$. Because the real s axis is the steepest-descent path passing through $s = 0$ in the s plane, we can obtain

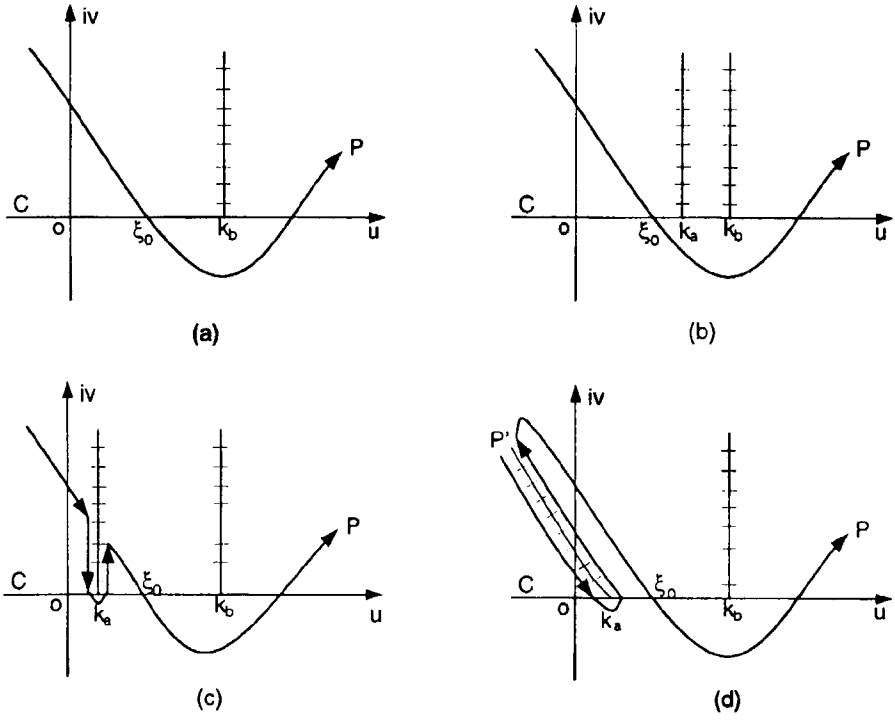

Figure 2. The steepest-descent paths and the branch cuts.

the steepest-descent path in the ξ plane by setting s to be real. Consequently,

$$v = \frac{\pm(k_b - u\sin\theta_0)(u - k_b\sin\theta_0)}{\sqrt{(k_b - u\sin\theta_0)^2 + (u - k_b\sin\theta_0)^2 + 2\sin\theta_0(k_b - u\sin\theta_0)(u - k_b\sin\theta_0)}} \tag{15}$$

in which $\xi = u + iv$. We must choose " $-$ " in (15) to ensure Λs^2 to be positive. Therefore the steepest-descent path P passing through the saddle point in the ξ plane is shown in Fig. 2, which intersects with the u axis at $k_b\sin\theta_0$ and $k_b/\sin\theta_0$. Note that vertical branch cuts chosen in Fig. 2 are used to judge when the contribution of the branch points should be considered in the integration. In numerical codes, however, the standard Sommerfeld cuts are used.

From Fig. 2(a), the steepest-descent path P will never cross the branch cut of k_b. Thus k_b has no contribution to the integral in any case.

We remark that the upper half space is usually a free space in our modeling. Hence $k_a < k_b$. In addition,

$$0 \leq \sin\theta_0 \leq \frac{W}{\sqrt{W^2+4h^2}}$$

from Fig. 1. So it is possible for both $k_a < k_b \sin\theta_0$ and $k_a > k_b \sin\theta_0$ if $W/\sqrt{W^2+4h^2} > k_a/k_b$.

When $k_a > k_b \sin\theta_0$, the steepest-descent path P will not cross the branch cut of k_a, as depicted in Fig. 2(b). In this case, the original integration path C will be directly deformed to P. After some mathematical derivation, we have

$$I(m,n) = I_S = e^{ik_b\bar{\rho}_{mn}} \int_{-\infty}^{+\infty} \frac{\beta_b - \beta_a}{\beta_b(\beta_b+\beta_a)} \times \exp\left[v\bar{\rho}_{mn}\frac{u-k_b\sin\theta_0}{k_b-u\sin\theta_0}\right]\left(1+i\frac{dv}{du}\right)du \tag{16}$$

in which $\beta_a = \sqrt{k_a^2-(u+iv)^2}$, and β_b and dv/du can be directly given by

$$\beta_b = \frac{k_b - u\sin\theta_0}{\cos\theta_0} - i\frac{u\cos\theta_0}{k_b-u\sin\theta_0}v, \tag{17}$$

$$\frac{dv}{du} = \frac{(k_b-u\sin\theta_0)[k_b(1+\sin^2\theta_0)-2u\sin\theta_0]-v^2\cos^2\theta_0}{(k_b-u\sin\theta_0)^2(u-k_b\sin\theta_0)}v. \tag{18}$$

In the integrand, v is replaced by (15). We remark that β_a and β_b should be in different Riemann sheets on the steepest-descent path: $\mathrm{Im}\,(\beta_a) < 0$ and $\mathrm{Im}\,(\beta_b) > 0$ when $u < 0$; $\mathrm{Im}\,(\beta_a) > 0$ and $\mathrm{Im}\,(\beta_b) < 0$ when $0 < u < \xi_0$; $\mathrm{Im}\,(\beta_a) > 0$ and $\mathrm{Im}\,(\beta_b) > 0$ when $u > \xi_0$. Obviously, (17) satisfies the above requirement. From (16), the integrand contains a rapidly decaying function $\exp(\cdot)$ which has a maximum value at the saddle point. Hence the integral I_S can be rapidly computed by setting a short integration interval near the saddle point.

When $k_a = k_b \sin\theta_0$, it defines a critical angle θ_c:

$$\theta_c = \sin^{-1}\frac{k_a}{k_b} \tag{19}$$

which will be discussed later in detail. This critical angle has a definite physical significance. When the plane wave is incident from space b to space

a at the angle θ_c, the refractive wave will propagate along the interface, i.e., a total internal reflection has occurred. Thus, θ_c is just the total internal reflection angle.

Finally, when $k_a < k_b \sin\theta_0$, the steepest-descent path P will cross the branch cut of k_a. In this case, we cannot deform C simply to P but we have to add the integral around the branch cut, as shown in Fig. 2(c). Therefore,

$$I(m,n) = I_S + I_B \tag{20}$$

in which I_B is the contribution from the branch point k_a. From Fig. 2(c), I_B can be expressed by the integrals on the branch cut in different Riemann sheets:

$$I_{B1} = \int_{v_a}^{0} \frac{1}{\beta_b}\left(\frac{\beta_b-\beta_a}{\beta_b+\beta_a} - \frac{\beta_b+\beta_a}{\beta_b-\beta_a}\right) e^{-i\beta_b(z_m+z_n)} e^{(-v+ik_a)|x_m-x_n|}(-i)dv \tag{21}$$

$$= -\frac{i4}{k_b^2-k_a^2}\int_0^{v_a} \beta_a e^{i(\beta_b|z_m+z_n|+k_a|x_m-x_n|)} e^{-v|x_m-x_n|}dv \tag{22}$$

where $\beta_a = \sqrt{v^2 - i2k_a v}$, $\beta_b = \sqrt{k_b^2 - k_a^2 + v^2 - i2k_a v}$, and

$$v_a = v(k_a) = \frac{(k_b - k_a\sin\theta_0)(k_b\sin\theta_0 - k_a)}{\cos\theta_0\sqrt{k_a^2+k_b^2-2k_ak_b\sin\theta_0}}. \tag{23}$$

Obviously $v_a > 0$ when $k_a < k_b\sin\theta_0$.

To save the computation time involved in the branch cut integral, we deform the integral around the branch cut onto the path of steepest descent passing through k_a. To do so, we find the direction of steepest descent at the point k_a first. From (11),

$$h_1'(k_a) = -i\frac{\bar{\rho}_{mn}}{\Lambda}\left(\frac{k_a}{\sqrt{k_b^2-k_a^2}}\cos\theta_0 - \sin\theta_0\right).$$

When $k_a < k_b\sin\theta_0$, $h_1'(k_a)$ can be written as

$$h_1'(k_a) = i\rho_0 = \rho_0 e^{i\frac{\pi}{2}} \qquad (\rho_0 > 0).$$

Letting $\xi - k_a = \rho e^{i\theta}$, then we have

$$h_1(\xi) - h_1(k_a) = h_1'(k_a)(\xi - k_a) = \rho_0\rho e^{i(\theta+\frac{\pi}{2})} \qquad (\xi \to k_a).$$

Hence the direction of steepest descent at k_a is $\theta + \frac{\pi}{2} = \pi$, i.e., $\theta = \frac{\pi}{2}$, which is useful for judging the correct branch of the steepest-descent path passing through k_a. Next, we make another change of variable:

$$-s = h_1(\xi) - h_1(k_a) = i\frac{\bar{\rho}_{mn}}{\Lambda}(\beta_b \cos\theta_0 + \xi \sin\theta_0 - k_c) \tag{24}$$

in which $k_c = \sqrt{k_b^2 - k_a^2}\cos\theta_0 + k_a \sin\theta_0$. Like the saddle point, when s is real, we will obtain the steepest-descent path P' in the $\xi-$ plane:

$$v = \frac{\pm(k_c - u\sin\theta_0)\sqrt{(u - k_c\sin\theta_0)^2 + (k_c^2 - k_b^2)\cos^2\theta_0}}{\sqrt{(k_c - u\sin\theta_0)^2 + (u - k_c\sin\theta_0)^2 + 2\sin\theta_0(k_c - u\sin\theta_0)(u - k_c\sin\theta_0)}} \tag{25}$$

in which we choose "+" to ensure that the direction of steepest descent is $+\frac{\pi}{2}$. We depict P' in Fig. 2(d). Note that P' is above P because $|v'| < |v|$ when $u = 0$. That is to say, P' and P has no intersecting point. Then we can deform the original contour C onto $P + P_1 + P_2$, as shown in Fig. 2(d). The integral along $P_1 + P_2$ can be expressed as the integration on the steepest-descent path passing through k_a in different Riemann sheets. After some derivations, we have

$$I_{B2} = -\frac{4}{k_b^2 - k_a^2} e^{ik_c\bar{\rho}_{mn}} \int_{-\infty}^{k_a} \beta_a \times \exp\left[v\bar{\rho}_{mn}\frac{u - k_c\sin\theta_0}{k_c - u\sin\theta_0}\right]\left(1 + i\frac{dv}{du}\right)du \tag{26}$$

in which

$$\beta_b = \frac{k_c - u\sin\theta_0}{\cos\theta_0} - i\frac{u\cos\theta_0}{k_c - u\sin\theta_0}v, \tag{27}$$

$$\frac{dv}{du} = \frac{(u - k_c\sin\theta_0)[(k_c - u\sin\theta_0)^2 - v^2\cos^2\theta_0]v}{(k_c - u\sin\theta_0)^2[(u - k_c\sin\theta_0)^2 + (k_c^2 - k_b^2)\cos^2\theta_0]} - \frac{v\sin\theta_0}{k_c - u\sin\theta_0} \tag{28}$$

and v is shown in (25). Note that β_b is not included in (26) but it will be used in the computation of $K_n(x, z)$, as shown in (41). Again, we remark that β_a and β_b should be in different Riemann sheets in the steepest-descent path passing through k_a: $\mathrm{Im}(\beta_a) > 0$ and $\mathrm{Im}(\beta_b) > 0$ when

$u < 0$; $\mathrm{Im}(\beta_a) < 0$ and $\mathrm{Im}(\beta_b) < 0$ when $u > 0$. Obviously, (27) satisfies the above requirement. From (26), I_{B2} can be rapidly computed because a similar exponentially decaying function to (16) exists in the integrand.

3.2 Integral $K_n(x, z)$

For the integral $K_n(x, z)$, we consider two cases: $z = 0$ and $z > 0$. From (10), $K_n(x, 0)$ can be reduced to

$$K_n(x,0) = \int_{-\infty}^{+\infty} \beta_b^{-1} T e^{-i\beta_b z_n} e^{i\xi(x-x_n)} d\xi \tag{29}$$

which has the same form as $I(m, n)$ after the following replacement: $z_n \to z_m + z_n$, $x - x_n \to x_m - x_n$, $T \to R$. Hence, we can use the same method described above to treat $K_n(x, 0)$, except that the range for $\sin\theta_0$ changes to

$$0 \le \sin\theta_0 \le \frac{X_{max}}{\sqrt{X_{max}^2 + h^2}}.$$

For the general case that $z > 0$, we consider the exponential term of (10) to obtain the saddle point

$$\Lambda h_2(\xi) = i\left(\beta_a z + \beta_b |z_n| + \xi |x - x_n|\right). \tag{30}$$

From $h_2'(\xi_0) = 0$, we get the equation for the saddle point ξ_0:

$$\frac{\xi_0}{\beta_a} z + \frac{\xi_0}{\beta_b} |z_n| = |x - x_n|. \tag{31}$$

It can be easily shown that the solution for the above equation is

$$\xi_0 = k_a \sin\theta_a = k_b \sin\theta_b \tag{32}$$

in which θ_b and θ_a are the incident and refractive angles when a plane wave propagates from (x_n, z_n) to (x, z), as shown in Fig. 3. Here, Snell's law has been used in (32). Substituting (32) into (31) yields

$$z \tan\theta_a + |z_n| \tan\theta_b = |x - x_n| \tag{33}$$

which satisfies the physical requirement shown in Fig. 3. This also shows the validity of the solution (32). Considering Snell's law, (33) gives a fourth-ordered algebraic equation for $\tan\theta_b$:

$$(\tan\theta_b)^4 + c_1(\tan\theta_b)^3 + c_2(\tan\theta_b)^2 + c_3(\tan\theta_b) + c_4 = 0 \tag{34}$$

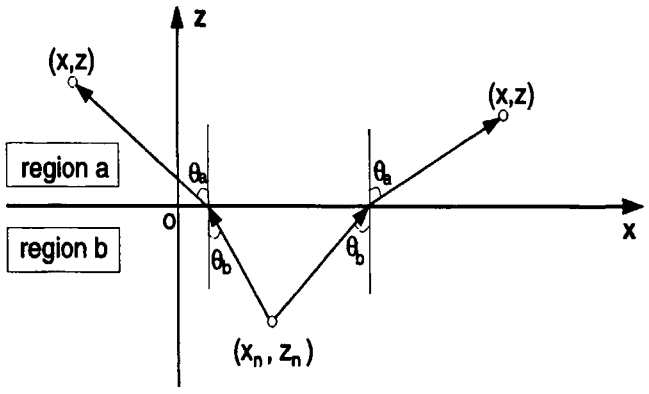

Figure 3. The propagation of plane wave from the source point to the field point.

where

$$c_1 = -\frac{2|x-x_n|}{|z_n|}, \qquad c_2 = \frac{(1-p)(x-x_n)^2 + z^2 - pz_n^2}{(1-p)z_n^2},$$

$$c_3 = \frac{2p|x-x_n|}{(1-p)|z_n|}, \qquad c_4 = -\frac{p(x-x_n)^2}{(1-p)z_n^2},$$

in which $p = k_a^2/k_b^2$. Equation (34) has a closed-form solution to $\tan\theta_b$, and hence, the saddle point ξ_0.

To obtain the steepest-descent path passing through ξ_0, a similar transform to (13) is made. Then we have

$$i\Lambda s^2 = \sqrt{k_a^2 - \xi^2}z + \sqrt{k_b^2 - \xi^2}|z_n| + \xi|x-x_n| - \frac{k_a z}{\cos\theta_a} - \frac{k_b|z_n|}{\cos\theta_b}. \tag{35}$$

When s is real, (35) will give the exact governing equation for the steepest-descent path in the ξ plane:

$$A_1^2 - A_2^2 - 2A_3A_5 - 2A_4A_6 + A_5^2 - A_6^2 = 0, \tag{36}$$

$$A_1A_2 + A_3A_6 - A_4A_5 - A_5A_6 = 0 \tag{37}$$

in which

$$A_1 = (k_a z)^2 - (k_b z_n)^2 + (z^2 - z_n^2)(v^2 - u^2)$$

$$A_2 = 2(z^2 - z_n^2)uv$$

$$A_3 = (k_a z)^2 + (k_b z_n)^2 + (z^2 + z_n^2)(v^2 - u^2)$$

$$A_4 = 2(z^2 + z_n^2)uv$$

$$A_5 = \left(|x - x_n|u - \frac{k_a z}{\cos\theta_a} - \frac{k_b|z_n|}{\cos\theta_b}\right)^2 - (\Lambda_0 + |x - x_n|v)^2$$

$$A_6 = 2(\Lambda_0 + |x - x_n|v)\left(|x - x_n|u - \frac{k_a z}{\cos\theta_a} - \frac{k_b|z_n|}{\cos\theta_b}\right)$$

and $\Lambda_0 = \Lambda s^2$. Hence, (36) and (37) are coupled equations about u and v with respect to the parameter Λ_0.

From (36) and (37), one sees that these equations are so complicated that v cannot be expressed in terms of u in closed form. Therefore it would be time consuming if we integrated along the exact steepest-descent path because v will have to be evaluated numerically in each integration step.

Now we consider an approximate method to determine the steepest-descent path. When z is large, the leading-order approximation of the method of steepest descent will give a good evaluation to the integral, which will be discussed in the next section. When z is small, (10) can be rewritten as

$$K_n(x, z) = \int_{-\infty}^{+\infty} \beta_b^{-1} T e^{i\beta_a z} e^{i(\beta_b|z_n| + \xi|x - x_n|)} d\xi \tag{38}$$

in which $\exp(i\beta_a z)$ is regarded as a part of T. Following the derivation in Case A, we have

$$K_S = 2e^{ik_b\bar{\rho}_n} \int_{-\infty}^{+\infty} \frac{e^{i\beta_a z}}{\beta_b + \beta_a} \exp\left[v\bar{\rho}_n \frac{u - k_b \sin\theta_0}{k_b - u\sin\theta_0}\right]\left(1 + i\frac{dv}{du}\right) du, \tag{39}$$

$$K_{B1} = i2\int_0^{v_a} \left(\frac{e^{i\beta_a z}}{\beta_b + \beta_a} - \frac{e^{-i\beta_a z}}{\beta_b - \beta_a}\right) e^{i(\beta_b|z_n| + k_a|x - x_n|)} e^{-v|x - x_n|} dv, \tag{40}$$

$$K_{B2} = 2e^{ik_c\bar{\rho}_n} \int_{-\infty}^{k_a} \left(\frac{e^{i\beta_a z}}{\beta_b + \beta_a} - \frac{e^{-i\beta_a z}}{\beta_b - \beta_a}\right) \times \exp\left[v\bar{\rho}_n \frac{u - k_c \sin\theta_0}{k_c - u\sin\theta_0}\right]\left(1 + i\frac{dv}{du}\right) du \tag{41}$$

in which $\bar{\rho}_n = \sqrt{(x - x_n)^2 + z_n^2}$, and $\theta_0 = \sin^{-1}|x - x_n|/\bar{\rho}_n$.

To verify the presented formulations, we first consider $I(m, n)$ with $R = 1$ which has a closed form

$$I(m, n) = \pi H_0^{(1)}(k_b\bar{\rho}_{mn}).$$

When $|z_m + z_n| = \lambda$ (Here and in the following, λ is the wave length), the computation results from the original integration path and steepest-descent paths and their comparison with the exact value are shown in Fig. 4. Here, the Gaussian quadrature method is used for the numerical integration, and x represents $|x_m - x_n|$. In the result from the original contour, a precision of 0.0001 is needed to obtain a comparable result with the exact value. The result from the steepest-descent path, however, needs only a precision of 0.01, as shown in Fig. 4. In this figure, 200 integrals at different points have been included. The CPU time used in the original contour is 6.665 seconds; however the CPU time used in the steepest-descent path is only 0.150 second.

For the general case of R, when $|z_m + z_n| = 4\lambda$, $z = 0.1\lambda$, $\epsilon_b = 4$ and $\epsilon_a = 1$, the computation results of $I(m,n)$ and $K_n(x,z)$ from the original integration path and steepest-descent paths are shown in Figs. 5 and 6. The comparisons of their CPU time are illustrated in Tab. 1. From Fig. 5, the results computed by the integral along the original contour has a little oscillation when x is small. This is because the current precision (0.0001) for the numerical integral is not enough. When it changes to 0.00001, the computation results fit very well but the CPU time becomes much higher. In addition, we also considered a lot of computations for different $|z_m + z_n|$ and z. Results show that when $|z_m + z_n|$ and z become larger, the CPU time needed in the original contour integrals is higher. From Tab. 1, the CPU time can be greatly reduced by integration along the steepest-descent paths.

4. METHOD OF STEEPEST DESCENT

In Section 3, we deform the original contour C onto the steepest-descent paths to speed up the numerical integration. However, when the unknowns N increases, the CPU time involved in the computation of the integrals becomes tremendous. In this section, we will discuss the asymptotic expansion of these integrals based on the method of steepest descent.

4.1 Integral $I(m,n)$

From the knowledge in Section 3, the main contribution to $I(m,n)$ comes from the saddle point ξ_0. The branch point k_b has no contribution and only when $k_a < k_b \sin\theta_0$ that the other branch point k_a has contribution to $I(m,n)$.

The saddle point shown in (12) will change to $s = 0$ in the s plane after the transform (13). This implies that most of the contributions to the

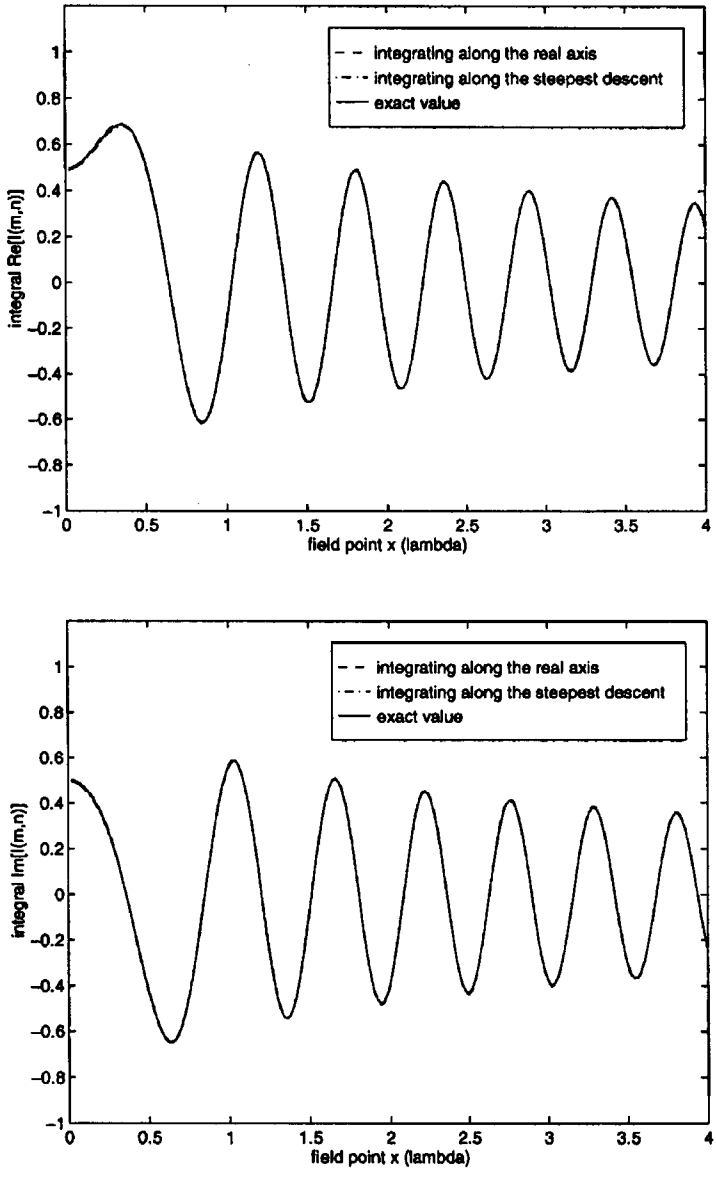

Figure 4. The computation results of integral $I(m, n)$ with $R = 1$ from the numerical integration methods. (a) Real part; (b) Imaginary part.

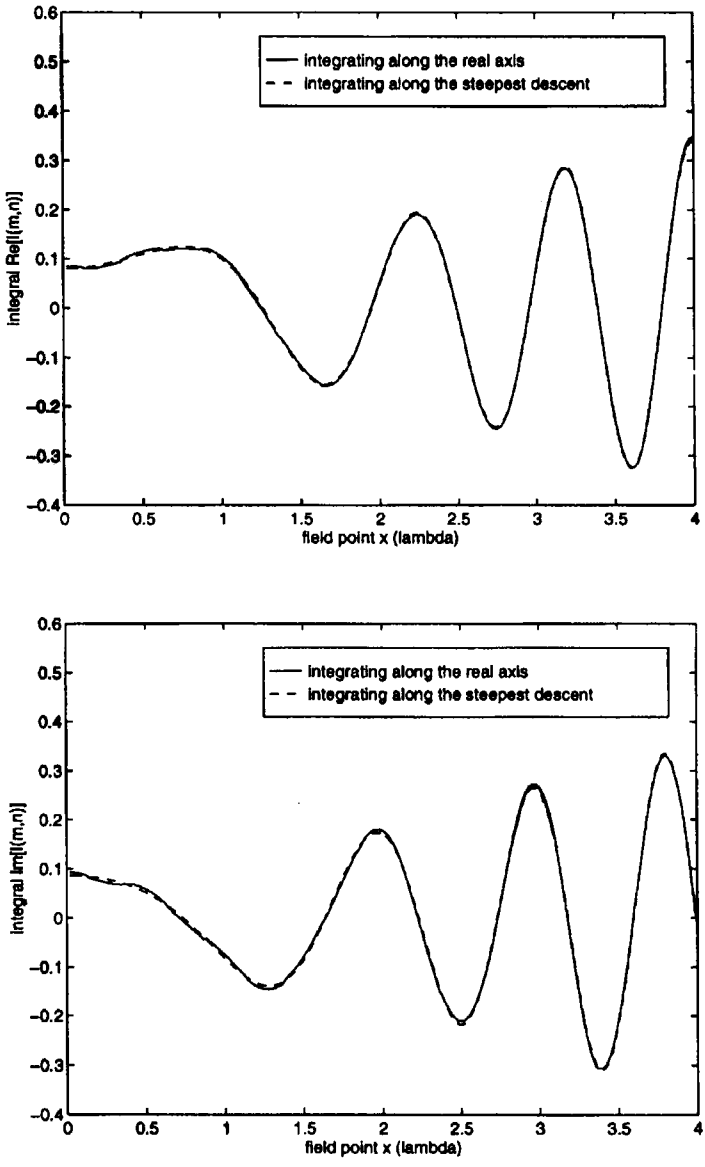

Figure 5. The computation results of integral $I(m, n)$ from the numerical integration methods. (a) Real part; (b) Imaginary part.

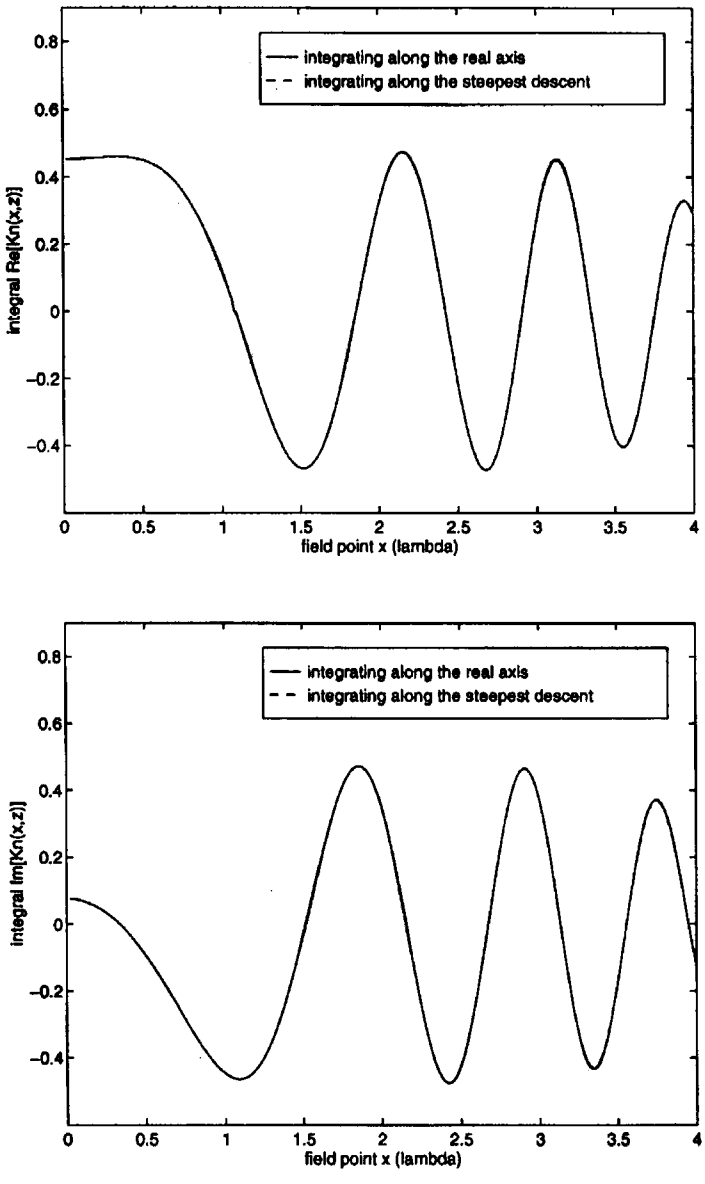

Figure 6. The computation results of integral $K_n(x, z)$ from the numerical integration methods. (a) Real part; (b) Imaginary part.

integral	$I(m,n)$		$K_n(x,z)$	
method	original contour	steepest descent path	original contour	steepest descent path
CPU time(s)	18.9079	0.5805	4.5066	0.6260

Table 1. The comparison of CPU time used in the computation of integrals.

integral I_S are from around $s = 0$. After expanding the integrand into a Taylor series about the origin, one obtains [31]

$$I_S \sim e^{\Lambda h_1(\xi_0)} \sqrt{\frac{\pi}{\Lambda}} \left[F(0) + \frac{F''(0)}{4\Lambda} + \cdots \right]. \tag{42}$$

in which

$$F(s) = f(\xi)\frac{d\xi}{ds} = \frac{R(\xi)}{\beta_b}\frac{d\xi}{ds}. \tag{43}$$

When $s = 0$,

$$F(0) = \frac{R(\xi_0)}{k_b \cos\theta_0} \sqrt{\frac{-2}{h_1''(\xi_0)}}. \tag{44}$$

Considering

$$\Lambda h_1''(\xi_0) = -i\bar{\rho}_{mn}/(k_b \cos^2\theta_0)$$

we get the leading-order approximation for I_S:

$$I_{S0} = R(\xi_0)\sqrt{\frac{-i2\pi}{k_b\bar{\rho}_{mn}}} e^{ik_b\bar{\rho}_{mn}} \tag{45}$$

$$\approx \pi R(\xi_0) H_0^{(1)}(k_b\bar{\rho}_{mn}). \tag{46}$$

In the case when $k_b\bar{\rho}_{mn}$ is large, the leading-order approximation yields a good evaluation to the integral I_S. To estimate the contribution from the higher-order terms, we make the second-order derivative of (43):

$$F''(s) = \frac{d^2 f}{d\xi^2}\left(\frac{d\xi}{ds}\right)^3 + 3\frac{df}{d\xi}\frac{d\xi}{ds}\frac{d^2\xi}{ds^2} + f\frac{d^3\xi}{ds^3}. \tag{47}$$

After some complicated derivations, we obtain the formulation for $F''(0)$. Substituting it into (42) yields

$$I_{S1} = \frac{-iI_{S0}}{2k_b\bar{\rho}_{mn}}\left[(1-3\tan^2\theta_0)f_1 + f_2\tan^2\theta_0 - \frac{3}{4}\right] \tag{48}$$

which is the second-order term of the series. Here,

$$f_1 = 1 + 2\beta_{b0}/\beta_{a0},$$

$$f_2 = [\beta_{a0}\beta_{b0}(\beta_{b0}-\beta_{a0}) + (2\beta_{b0}+\beta_{a0})(3\beta_{a0}^2 + \beta_{a0}\beta_{b0} + \beta_{b0}^2)]/\beta_{a0}^3$$

and $\beta_{b0} = k_b\cos\theta_0$, $\beta_{a0} = \sqrt{k_a^2 - k_b^2\sin^2\theta_0}$.

We remark that the series (42) may be not convergent depending on the radius of the convergence of the Taylor's expansion for $F(s)$. When this radius, which is given by the distance of the nearest singularity to the origin in the s plane [31], becomes small, the series (42) will diverge. In this event, the higher-order terms are useless for the evaluation of the integral. This phenomenon can also be observed from the above formulas.

As mentioned in Section 3, there exists a critical angle θ_c. At this angle, $\beta_{a0} = 0$. Hence $f_1, f_2 \to \infty$ and furthermore $I_{S1} \to \infty$. The reason why the series is divergent at the critical angle is because the distance of the nearest singularity to the origin in the s plane equals zero. It is easy to imagine that near the critical angle θ_c:

$$|k_a - k_b\sin\theta_0| \le \delta \tag{49}$$

the series (42) is also divergent, just as shown in Fig. 7. Here, $|z_m + z_n| = 0.5\lambda$, and other parameters are the same as those in Fig. 5. From Fig. 7, we can also see that there is little improvement for the second-order term beyond the scope given by (49).

Next, we consider the contribution from the branch point k_a. Using the similar procedure to the saddle point and making the transform (24), one obtains [31]

$$I_{B0} = e^{\Lambda h_1(k_a)}\bar{F}(0)\frac{\Gamma(\frac{3}{2})}{\Lambda^{3/2}} \tag{50}$$

in which

$$\bar{F}(s) = -\frac{4}{k_b^2 - k_a^2}(k_a^2 - \xi^2)^{\frac{1}{2}}s^{-\frac{1}{2}}\frac{d\xi}{ds}. \tag{51}$$

After some derivations, we get the leading-order approximation

$$I_{B0} = \frac{2\sqrt{2\pi k_a}}{\sqrt[4]{k_b^2 - k_a^2}}\frac{\exp\left[i(k_a|x_m - x_n| + \sqrt{k_b^2 - k_a^2}|z_m + z_n| + \frac{\pi}{4})\right]}{\left(\sqrt{k_b^2 - k_a^2}|x_m - x_n| - k_a|z_m + z_n|\right)^{3/2}}, \tag{52}$$

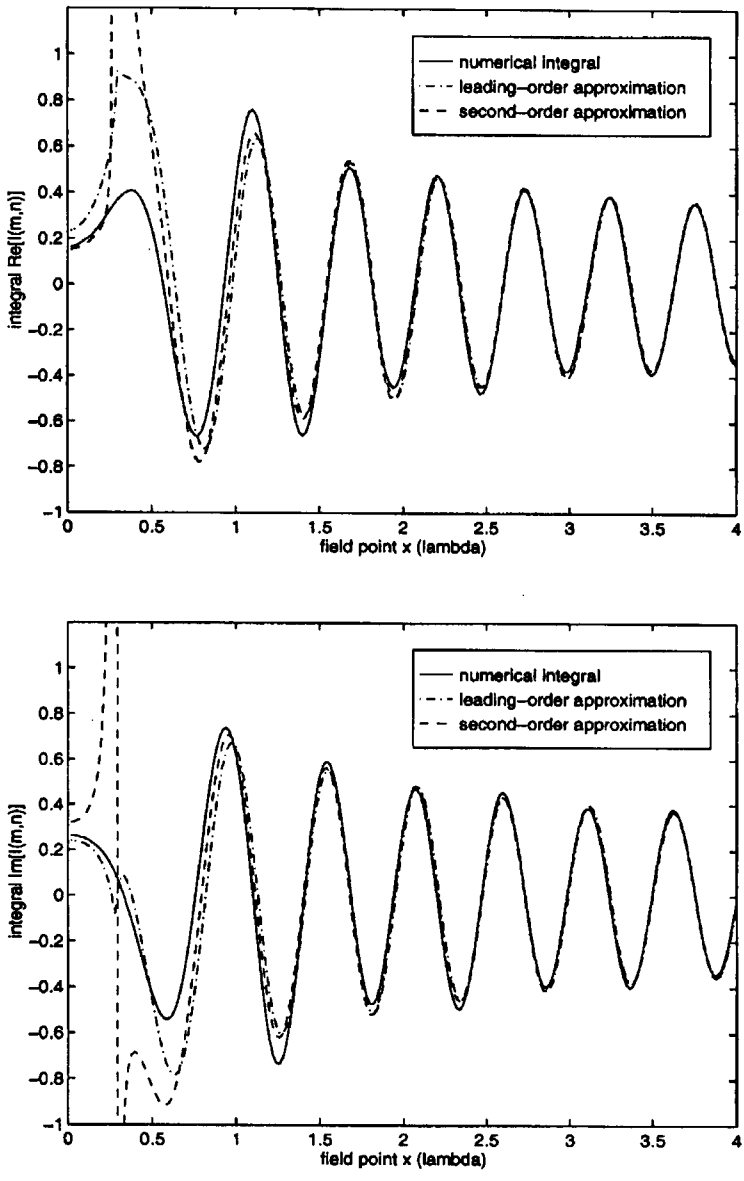

Figure 7. The computation results of integral $I(m, n)$ from the leading-order and second-order approximations. (a) Real part; (b) Imaginary part.

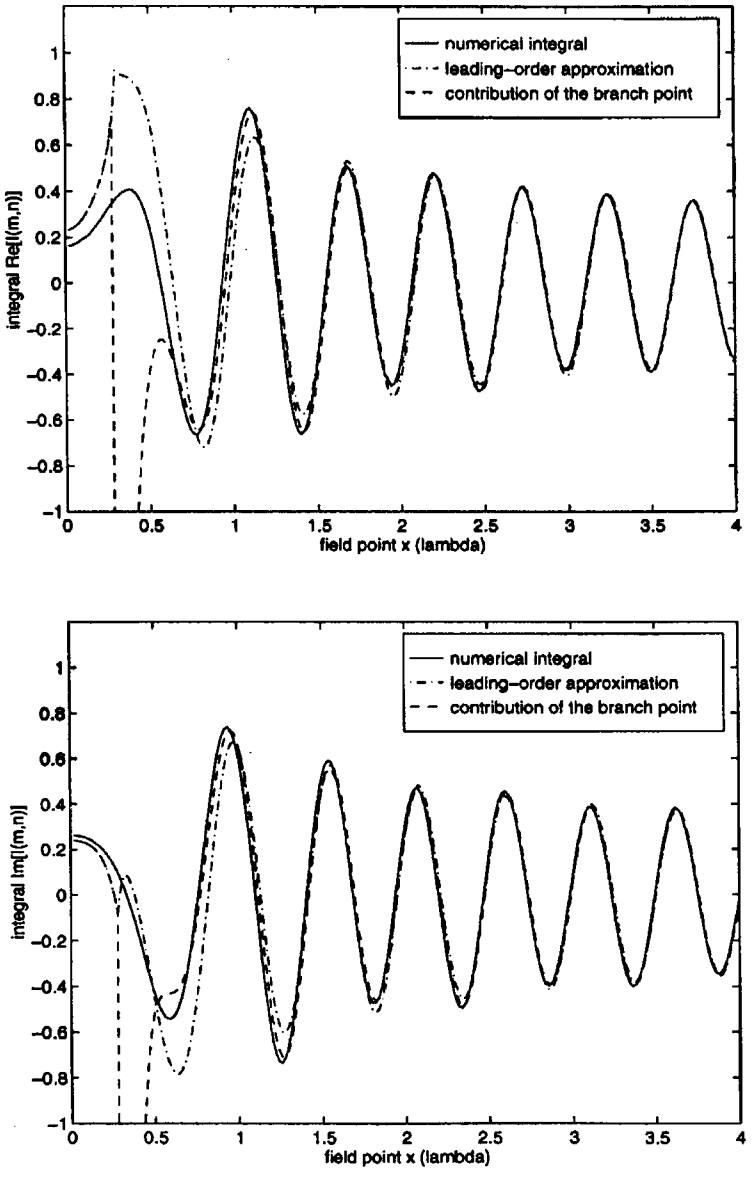

Figure 8. The computation results of integral $I(m, n)$ from the leading-order approximation and the contribution of the branch point. (a) Real part; (b) Imaginary part.

in which we have considered

$$\sqrt{k_b^2 - k_a^2}|x_m - x_n| \geq k_a|z_m + z_n| \tag{53}$$

when $k_a \leq k_b \sin\theta_0$. Again, at the critical angle θ_c, the equality of (53) is true. Thus $I_{B0} \to \infty$. This implies that the leading-order approximation of the contribution from the branch point k_a is invalid near the critical angle. Beyond this region, I_{B0} also gives little improvement to the integral $I(m,n)$, as shown in Fig. 8, in which $|z_m + z_n| = 0.5\lambda$.

4.2 Integral $K_n(x,z)$

When $z = 0$, the leading-order approximation for (29) is easily obtained by using the similar method to that of $I(m,n)$

$$K_n(x,0) \approx \pi T(\xi_0) H_0^{(1)}(k_b \bar{\rho}_n). \tag{54}$$

In addition, the second-order term and the contribution from the branch point k_a to the integral $K_n(x,0)$ can also be evaluated. From the above analysis, however, the two terms will break down near the critical angle θ_c, and have only little contribution to the integral compared with the leading-order term beyond the region. Hence, we will only consider the leading-order approximation.

In the general case that $z > 0$, the saddle point $\xi_0 = k_a \sin\theta_a = k_b \sin\theta_b$ will be determined by the fourth-ordered algebraic equation (34). Using a similar procedure to handle $I(m,n)$, we have

$$K_n(x,z) \approx T(\xi_0) \exp\left[i\left(\frac{k_a z}{\cos\theta_a} + \frac{k_b|z_n|}{\cos\theta_b}\right)\right] \sqrt{\frac{-i2\pi}{\frac{k_a z}{\cos\theta_a} q + \frac{k_b|z_n|}{\cos\theta_b}}} \tag{55}$$

$$\approx \pi T(\xi_0) H_0^{(1)}\left(\frac{k_a z}{\cos\theta_a} q + \frac{k_b|z_n|}{\cos\theta_b}\right) \exp\left[i(1-q)\frac{k_a z}{\cos\theta_a}\right] \tag{56}$$

in which

$$q = \frac{k_b^2 \cos^2\theta_b}{k_a^2 \cos^2\theta_a}.$$

In fact, when $z = 0, \theta_b = \theta_0$ from (33). Then (56) reduces to (54). Hence (56) is the general formulation to the integral $K_n(x,z)$.

5. UNIFORM ASYMPTOTIC EXPANSIONS

The asymptotic expansions of integrals $I(m,n)$ and $K_n(x,z)$ based on the method of steepest descent can greatly speed up the computation of these

integrals. However this method will break down near the critical angle θ_c, as stated in the above section. The reason causing the invalidity of the method is because the saddle point is too close to (or even coincides with) the branch point, and the radius of convergence of the Taylor series diminishes. In this section, we will consider the uniform asymptotic expansions [31, 32] of such integrals to overcome this shortcoming.

Generally speaking, the uniform asymptotic expansion method handles integrals that contain nearby critical points, for example, two nearby saddle points, the saddle point near a branch point, etc. [32]. When a branch point like k_a is close to the saddle point, the following integral

$$I = \int_C (\xi - k_a)^{\frac{1}{2}} g(\xi) e^{\Lambda h(\xi)} d\xi \tag{57}$$

has been well studied for its uniform asymptotic expansions [31, 32]. Here we only give its final result.

Using the transform (13), the saddle point ξ_0 changes to $s = 0$, and the branch point k_a to s_a. After approximating the integrand with a polynomial that interpolates the saddle point and branch point and then integrating by part, one obtains the leading-order approximation to the integral I [31]

$$I \cong \frac{e^{\Lambda[h(\xi_0)-s_a^2]}}{\sqrt{2\Lambda}} \left[\frac{\gamma_0}{(2\Lambda)^{1/4}} W_{\frac{1}{2}}(\sqrt{2\Lambda} s_a) + \frac{\gamma_1}{(2\Lambda)^{3/4}} W_{\frac{3}{2}}(\sqrt{2\Lambda} s_a) \right] \tag{58}$$

in which

$$W_\kappa(\sqrt{2\Lambda} s_a) = \int_{-\infty}^{+\infty} u^\kappa e^{-(\frac{u^2}{2} + \sqrt{2\Lambda} s_a u)} du \tag{59}$$

is so-called W-function [31]; and

$$\gamma_0 = G(s_a), \qquad \gamma_1 = \frac{G(s_a) - G(0)}{s_a}, \tag{60}$$

where

$$G(s) = \left(\frac{\xi - k_a}{s - s_a} \right)^{\frac{1}{2}} g(\xi) \frac{d\xi}{ds}. \tag{61}$$

Since the effect of branch point is taken into account in the above approximation, (58) is uniformly valid for all θ_0.

5.1 Integral $I(m, n)$

To obtain the uniform asymptotic approximation of the integral $I(m, n)$, we must match $I(m, n)$ with (57). From (4),

$$R = T - 1 = \frac{2\beta_b}{\beta_b + \beta_a} - 1 = \frac{2\beta_b}{k_b^2 - k_a^2} (\beta_b - \beta_a) - 1.$$

Then the integral $I(m,n)$ can be written as

$$I(m,n) = \frac{2}{k_b^2 - k_a^2}(I_b - I_a) - \pi H_0^{(1)}(k_b \bar{\rho}_{mn}) \tag{62}$$

in which

$$I_{a,b} = \int_{-\infty}^{+\infty} \beta_{a,b} e^{\Lambda h_1(\xi)} d\xi. \tag{63}$$

In the above two integrals, the branch point k_a is not included in I_b. In addition, we have shown that the other branch point k_b is always far away from the saddle point. Hence the integral I_b can be evaluated by the steepest-descent method. From Section 4, we have

$$I_b \approx \pi k_b^2 \cos^2\theta_0 H_0^{(1)}(k_b \bar{\rho}_{mn}). \tag{64}$$

For the other integral I_a:

$$I_a = \int_{-\infty}^{+\infty} (\xi - k_a)^{\frac{1}{2}} (-\xi - k_a)^{\frac{1}{2}} e^{\Lambda h_1(\xi)} d\xi \tag{65}$$

which matches (57) with

$$g(\xi) = (-\xi - k_a)^{\frac{1}{2}}. \tag{66}$$

From (60) and (61), we have

$$\gamma_0 = G(s_a) = \lim_{\xi \to k_a} \left(\frac{\xi - k_a}{s - s_a} \right)^{\frac{1}{2}} g(\xi) \frac{d\xi}{ds} \tag{67}$$

$$= -\frac{4 s_a}{h_1'(k_a)} \sqrt{\frac{k_a s_a}{h_1'(k_a)}}, \tag{68}$$

$$G(0) = \lim_{\xi \to \xi_0} \left(\frac{\xi - k_a}{s - s_a} \right)^{\frac{1}{2}} g(\xi) \frac{d\xi}{ds} \tag{69}$$

$$= \sqrt{2k_b} \cos\theta_0 \sqrt{\frac{-i(k_b^2 \sin^2\theta_0 - k_a^2)}{s_a}}, \tag{70}$$

in which

$$s_a^2 = i \left(k_b - k_a \sin\theta_0 - \sqrt{k_b^2 - k_a^2} \cos\theta_0 \right), \tag{71}$$

$$h_1'(k_a) = -i \left(\frac{k_a}{\sqrt{k_b^2 - k_a^2}} \cos\theta_0 - \sin\theta_0 \right). \tag{72}$$

To simplify the expressions for γ_0 and γ_1 and consider their limiting values when $\theta_0 \to \theta_c$, the critical angle, we let

$$g_0(t) = k_b - k_a t - \sqrt{(k_b^2 - k_a^2)(1 - t^2)}, \tag{73}$$

$$g_1(t) = t - k_a \sqrt{\frac{1 - t^2}{k_b^2 - k_a^2}}, \tag{74}$$

$$g_2(t) = (k_b^2 t^2 - k_a^2)(1 - t^2), \tag{75}$$

in which $t = \sin\theta_0$ and $t_c = \sin\theta_c = k_a/k_b$. It can be easily shown that the three simple functions have the following properties:

$$g_0(t) \geq 0; \quad g_0(t_c) = 0, \quad g_0'(t_c) = 0, \quad g_0''(t_c) \neq 0$$
$$g_1(t_c) = 0, \quad g_1'(t_c) \neq 0; \quad g_2(t_c) = 0, \quad g_2'(t_c) \neq 0.$$

Then γ_0 and γ_1 can be expressed as

$$\gamma_0 = \alpha_0 4\sqrt{k_a} \left(\frac{\sqrt{g_0}}{|g_1|}\right)^{\frac{3}{2}}, \tag{76}$$

$$\gamma_1 = \alpha_1 \left[4\sqrt{k_a} \left(\frac{\sqrt{g_0}}{|g_1|}\right)^{\frac{3}{2}} - \sqrt{2k_b} \left(\frac{|g_2|}{\sqrt{g_0}}\right)^{\frac{1}{2}}\right] / \sqrt{g_0} \tag{77}$$

where α_0 and α_1 are multi-value complex numbers:

$$\alpha_0 = e^{i\frac{(4m-1)\pi}{8}}, \quad \alpha_1 = e^{i\frac{(4m-3)\pi}{8}}, \quad (m = 1, 2, 3, 4).$$

At the critical angle θ_c, both γ_0 and γ_1 are limits of the type of "0/0". Using the properties of the above three functions, we obtain (see *Appendix*)

$$\lim_{\theta_0 \to \theta_c} \gamma_0 = \alpha_0 4\sqrt{k_a} \left(\frac{k_b^2 - k_a^2}{2k_b}\right)^{\frac{3}{4}}, \tag{78}$$

$$\lim_{\theta_0 \to \theta_c} \gamma_1 = \alpha_1 \frac{6k_a^2 - k_b^2}{k_b\sqrt{k_a}} \left(\frac{k_b^2 - k_a^2}{2k_b}\right)^{\frac{1}{4}}. \tag{79}$$

Hence the leading-order approximation of the integral I_a can be written as

$$I_a = \frac{\exp(ik_c\bar{\rho}_{mn})}{\sqrt{2\bar{\rho}_{mn}}} \times \left[\frac{\gamma_0}{(2\bar{\rho}_{mn})^{1/4}} W_{\frac{1}{2}}(\sqrt{2\bar{\rho}_{mn}} s_a) + \frac{\gamma_1}{(2\bar{\rho}_{mn})^{3/4}} W_{\frac{3}{2}}(\sqrt{2\bar{\rho}_{mn}} s_a)\right] \tag{80}$$

in which we have let $\Lambda = \bar{\rho}_{mn}$, and k_c is the same as that in (24).

From the special function theory [34], the W-function $W_\kappa(z)$ is related to the parabolic cylinder function $D_\kappa(z)$

$$W_\kappa(z) = \sqrt{2\pi} e^{\pm i\frac{\kappa\pi}{2} + \frac{z^2}{4}} D_\kappa(\pm iz) \tag{81}$$

And $D_\kappa(z)$ is associated with the Hermite function $H_\kappa(z)$

$$D_\kappa(z) = 2^{-\frac{\kappa}{2}} e^{-\frac{z^2}{4}} H_\kappa\left(\frac{z}{\sqrt{2}}\right). \tag{82}$$

Thus, the W-function can be expressed by the Hermite function. Considering (71) and (73), we obtain

$$W_\kappa(\sqrt{2\bar{\rho}_{mn}} s_a) = \sqrt{2\pi} 2^{-\frac{\kappa}{2}} e^{\pm i\frac{\kappa\pi}{2}} e^{ir^2} H_\kappa(\pm i^{\frac{1}{2}} r) \tag{83}$$

in which $r = \sqrt{\bar{\rho}_{mn} g_0}$ and $\kappa = \frac{1}{2}, \frac{3}{2}$. Substituting (83) into (80), we have

$$I_a = \sqrt{\frac{\pi}{\bar{\rho}_{mn}}} e^{ik_b \bar{\rho}_{mn}} \left[\frac{\gamma_0'}{(4\bar{\rho}_{mn})^{1/4}} H_{\frac{1}{2}}(\pm i^{\frac{1}{2}} r) + \frac{\gamma_1'}{(4\bar{\rho}_{mn})^{3/4}} H_{\frac{3}{2}}(\pm i^{\frac{1}{2}} r) \right], \tag{84}$$

where $\gamma_0' = \gamma_0 \alpha_1 / \alpha_0$ and $\gamma_1' = \gamma_1 \alpha_0 / \alpha_1$.

The Hermite function has been well studied [34]. An explicit series representation for $H_\kappa(z)$ can be written as

$$H_\kappa(z) = \frac{1}{2\Gamma(-\kappa)} \sum_{m=0}^{+\infty} \frac{(-1)^m \Gamma\left(\frac{m-\kappa}{2}\right)}{m!} (2z)^m, \quad |z| < \infty \tag{85}$$

which is valid for all possible arguments, but converges slowly when $|z|$ is large. For large argument $|z|$, $H_\kappa(z)$ has the following asymptotic expansions:

$$H_\kappa(z) = (2z)^\kappa \sum_{m=0}^{n} \frac{(-1)^m (-\kappa)_{2m}}{m!} (2z)^{-2m} + O(|z|^{-2n-2}) \tag{86}$$

which is valid for the sector of the complex plane $|\arg z| \leq \frac{3}{4}\pi$;

$$H_\kappa(z) = (2z)^\kappa \sum_{m=0}^{n} \frac{(-1)^m (-\kappa)_{2m}}{m!} (2z)^{-2m} - \frac{\sqrt{\pi}}{\Gamma(-\kappa)} e^{i\kappa\pi + z^2} z^{-\kappa-1} \times \sum_{m=0}^{n} \frac{(\kappa+1)_{2m}}{m!} (2z)^{-2m} + O(|z|^{-2n-2}) \tag{87}$$

for the sector of $\frac{\pi}{4} \le \arg z \le \frac{5}{4}\pi$; and

$$H_\kappa(z) = (2z)^\kappa \sum_{m=0}^{n} \frac{(-1)^m(-\kappa)_{2m}}{m!}(2z)^{-2m} - \frac{\sqrt{\pi}}{\Gamma(-\kappa)} e^{-i\kappa\pi+z^2} z^{-\kappa-1} \sum_{m=0}^{n} \frac{(\kappa+1)_{2m}}{m!}(2z)^{-2m} + O(|z|^{-2n-2}) \tag{88}$$

for the sector of $-\frac{5\pi}{4} \le \arg z \le -\frac{\pi}{4}$. Here, $(\kappa)_0 = 1$ and

$$(\kappa)_{2m} = \frac{\Gamma(\kappa+2m)}{\Gamma(\kappa)} = (\kappa)(\kappa+1)(\kappa+2)\cdots(\kappa+2m-1).$$

Equations (86)–(88) give a complete description of the behavior of the Hermite function for large $|z|$. These formulas do not contradict each other in their common regions of applicability, since the second terms of (87) and (88) are small compared to the first term if $-\frac{3}{4}\pi \le \arg z \le -\frac{\pi}{4}$ and $\frac{\pi}{4} \le \arg z \le \frac{3}{4}\pi$.

5.2. Integral $K_n(x, z)$

Similar to $I(m, n)$, the integral $K_n(x, z)$ can be written as two parts:

$$K_n(x, z) = \frac{2}{k_b^2 - k_a^2}(K_b - K_a) \tag{89}$$

in which

$$K_{a,b} = \int_{-\infty}^{+\infty} \beta_{a,b} e^{\Lambda h_2(\xi)} d\xi. \tag{90}$$

For K_b , the leading-order approximation of the steepest-descent method yields a good evaluation

$$K_b \approx \pi k_b^2 \cos^2\theta_b H_0^{(1)}\left(\frac{k_a z}{\cos\theta_a} q + \frac{k_b|z_n|}{\cos\theta_b}\right) \exp\left[i(1-q)\frac{k_a z}{\cos\theta_a}\right]. \tag{91}$$

For the integral K_a , we use the uniform asymptotic expansions. If we write K_a as

$$K_a = \int_{-\infty}^{+\infty} (\xi - k_a)^{\frac{1}{2}} g(\xi) e^{\Lambda h_2(\xi)} d\xi \tag{92}$$

we will have

$$h_2'(k_a) = \frac{-i}{\bar{\rho}_n} \lim_{\xi \to k_a} \left(\frac{\xi}{\beta_a} z + \frac{\xi}{\beta_b}|z_n| - |x - x_n|\right) \to \infty.$$

Then $\gamma_0 = 0$ from (68). Hence it is unreasonable because of the lack of an important term. Like the case in Section 4, when z is not large, (92) can be rewritten as

$$K_a = \int_{-\infty}^{+\infty} (\xi - k_a)^{\frac{1}{2}} \bar{g}(\xi) e^{\Lambda h_1(\xi)} d\xi \tag{93}$$

where

$$\bar{g}(\xi) = g(\xi) e^{i\beta_a z}. \tag{94}$$

In this case, K_a has a similar form to I_a. Consequently,

$$K_a = \sqrt{\frac{\pi}{\bar{\rho}_n}} e^{ik_b\bar{\rho}_n} \left[\frac{\bar{\gamma}_0'}{(4\bar{\rho}_n)^{1/4}} H_{\frac{1}{2}}(\pm i^{\frac{1}{2}} r) + \frac{\bar{\gamma}_1'}{(4\bar{\rho}_n)^{3/4}} H_{\frac{3}{2}}(\pm i^{\frac{1}{2}} r) \right], \tag{95}$$

in which

$$\bar{\gamma}_0' = \gamma_0' = \alpha_1 4\sqrt{k_a} \left(\frac{\sqrt{g_0}}{|g_1|} \right)^{\frac{3}{2}}, \tag{96}$$

$$\bar{\gamma}_1' = \alpha_0 \left[4\sqrt{k_a} \left(\frac{\sqrt{g_0}}{|g_1|} \right)^{\frac{3}{2}} - \sqrt{2k_b} \left(\frac{|g_2|}{\sqrt{g_0}} \right)^{\frac{1}{2}} e^{i\sqrt{k_a^2 - k_b^2 \sin^2\theta_0} z} \right] / \sqrt{g_0}. \tag{97}$$

When $\theta_0 = \theta_c$, $\bar{\gamma}_0' = \gamma_0', \bar{\gamma}_1' = \gamma_1'$, as shown in (78) and (79). We remark that $\sin\theta_0$ in K_a is different from that in I_a, which is defined as $\sin\theta_0 = |x - x_n|/\bar{\rho}_n$. And, $\bar{\rho}_{mn}$ appeared in K_a should be replaced by $\bar{\rho}_n$.

Now we verify the uniform asymptotic formulations. When $|z_m + z_n| = 0.5\lambda, z = 0$, $\epsilon_a = 1, \epsilon_b = 4$, the computed results of $I(m,n)$ and $K_n(x,z)$ from the uniform asymptotic solution, the leading-order approximation of the steepest-descent method, and the numerical integral are shown in Figs. 9 and 10. In this case, the critical angle appears at $x/\lambda = 0.5/\sqrt{3} \approx 0.29$. From Figs. 9 and 10, the leading-order approximations give a poor evaluation near the point. The uniform asymptotic solutions, however, give an excellent approximation.

When $|z_m + z_n| = \lambda$ and 4λ, the critical angle will appear at $x/\lambda = 1/\sqrt{3} \approx 0.58$ and $x/\lambda = 4/\sqrt{3} \approx 2.31$, respectively. In these events, the computations results of $I(m,n)$ and $K_n(x,z)$ are shown in Figs. 11–14, from which we can clearly see that the leading-order approximations break down while the uniform asymptotic solutions give good results.

In addition, the CPU time used in the above methods are illustrated in Tab. 2. Clearly, the CPU time can be greatly reduced by using the leading-order approximation and uniform asymptotic solution.

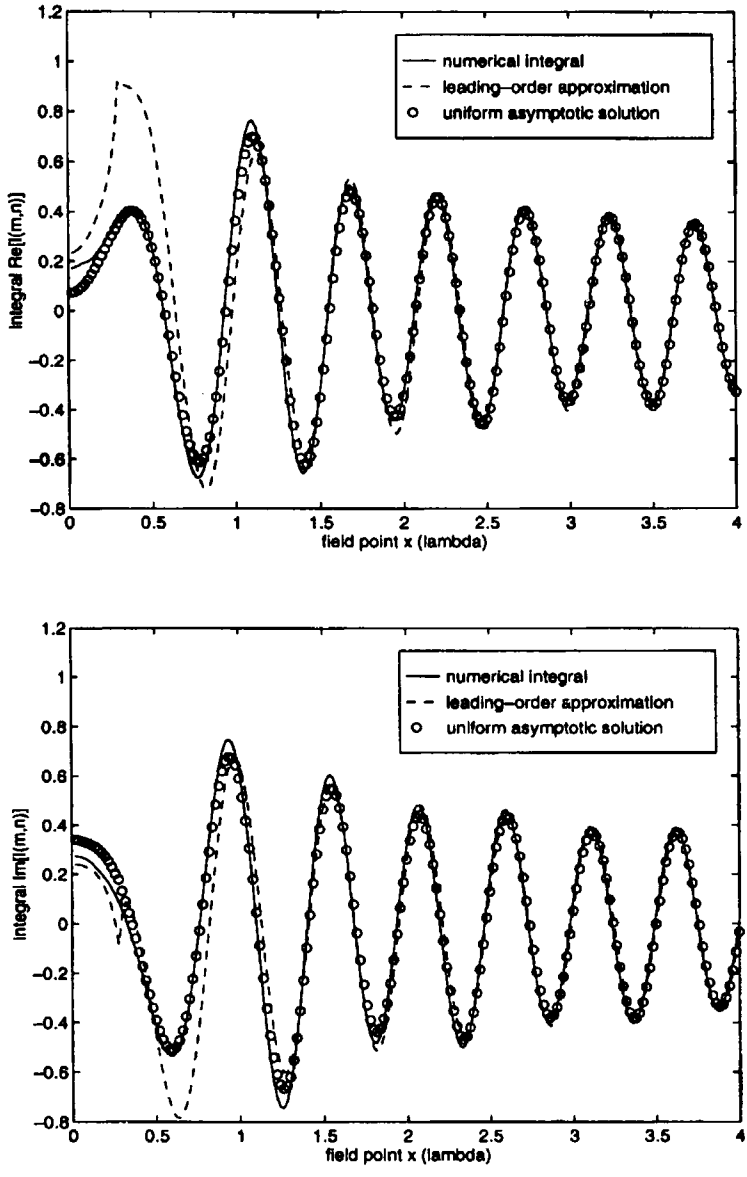

Figure 9. The computation results of integral $I(m,n)$ from the uniform asymptotic expansion method when $|z_m + z_n| = 0.5\lambda$. (a) Real part; (b) Imaginary part.

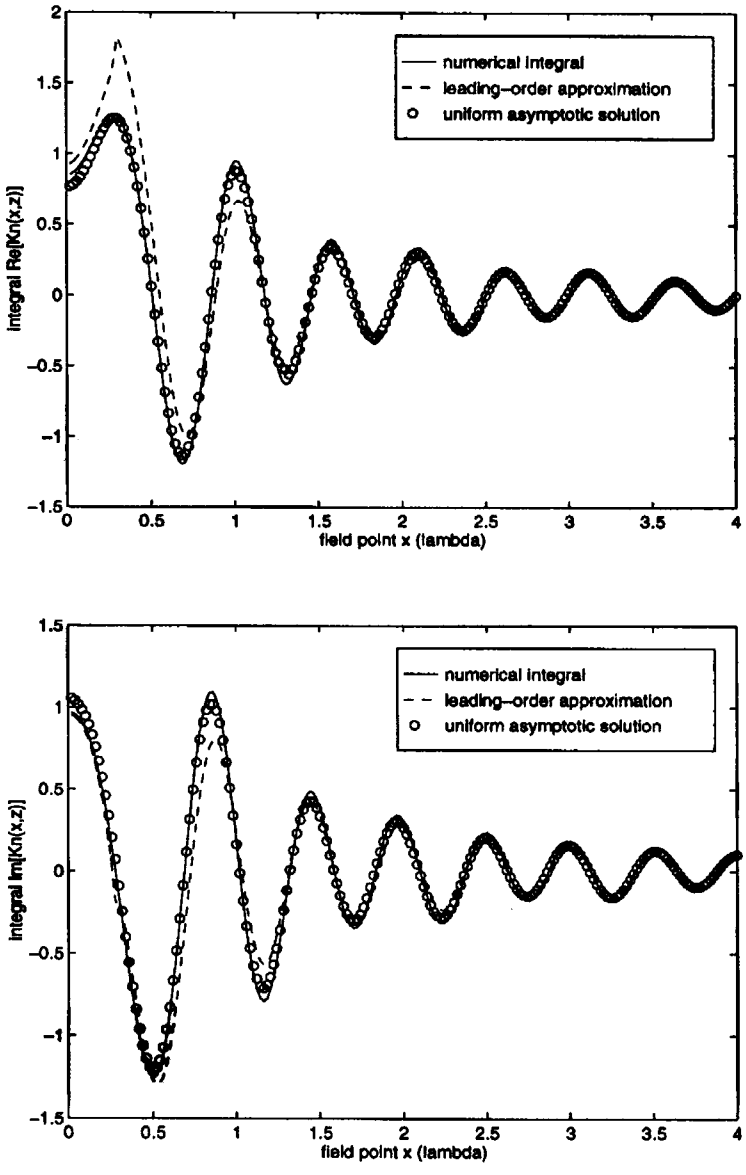

Figure 10. The computation results of integral $K_n(x, z)$ from the uniform asymptotic expansion method when $|z_n| = 0.5\lambda$. (a) Real Part; (b) Imaginary part.

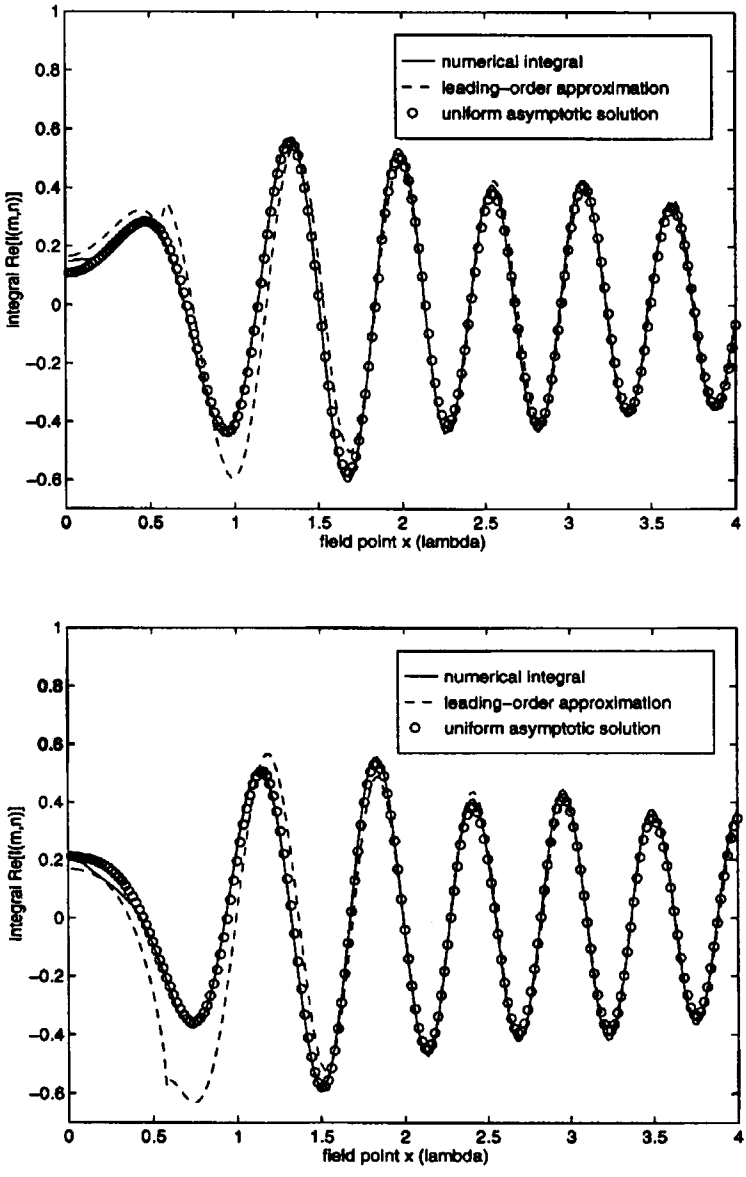

Figure 11. The computation results of integral $I(m, n)$ from the uniform asymptotic expansion method when $|z_m + z_n| = \lambda$. (a) Real part; (b) Imaginary part.

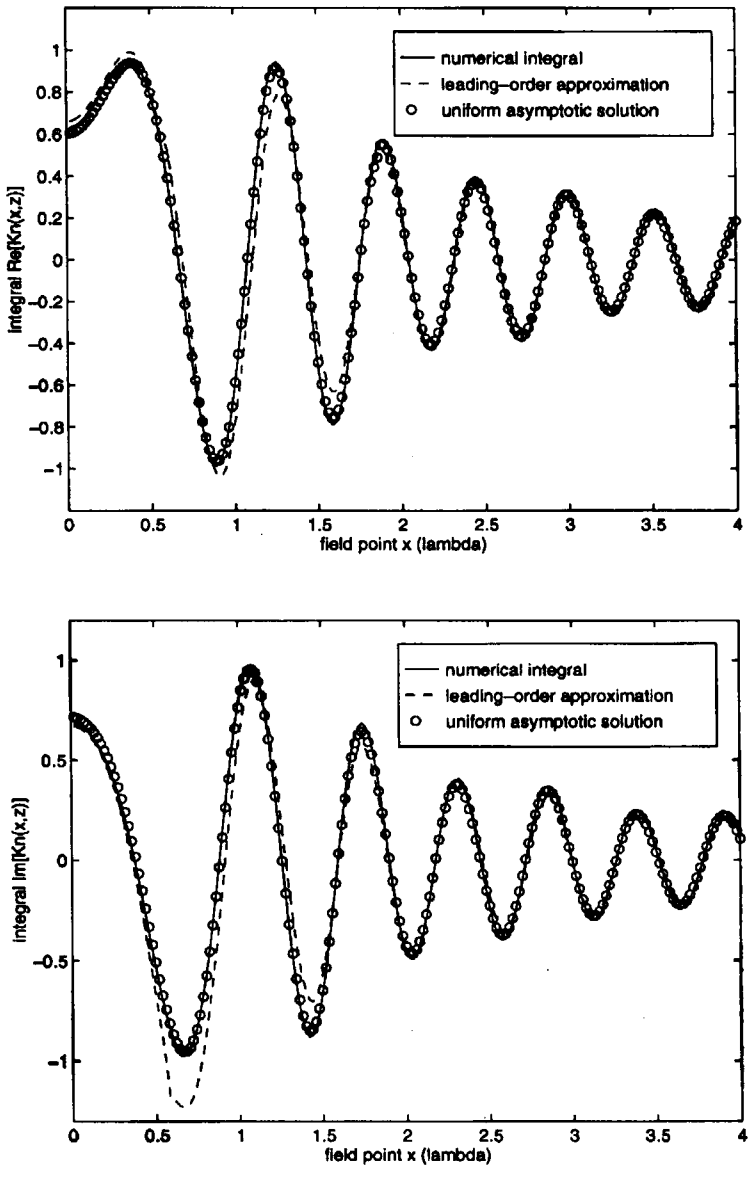

Figure 12. The computation results of integral $K_n(x, z)$ from the uniform asymptotic expansion method when $|z_n| = \lambda$. (a) Real part; (b) Imaginary part.

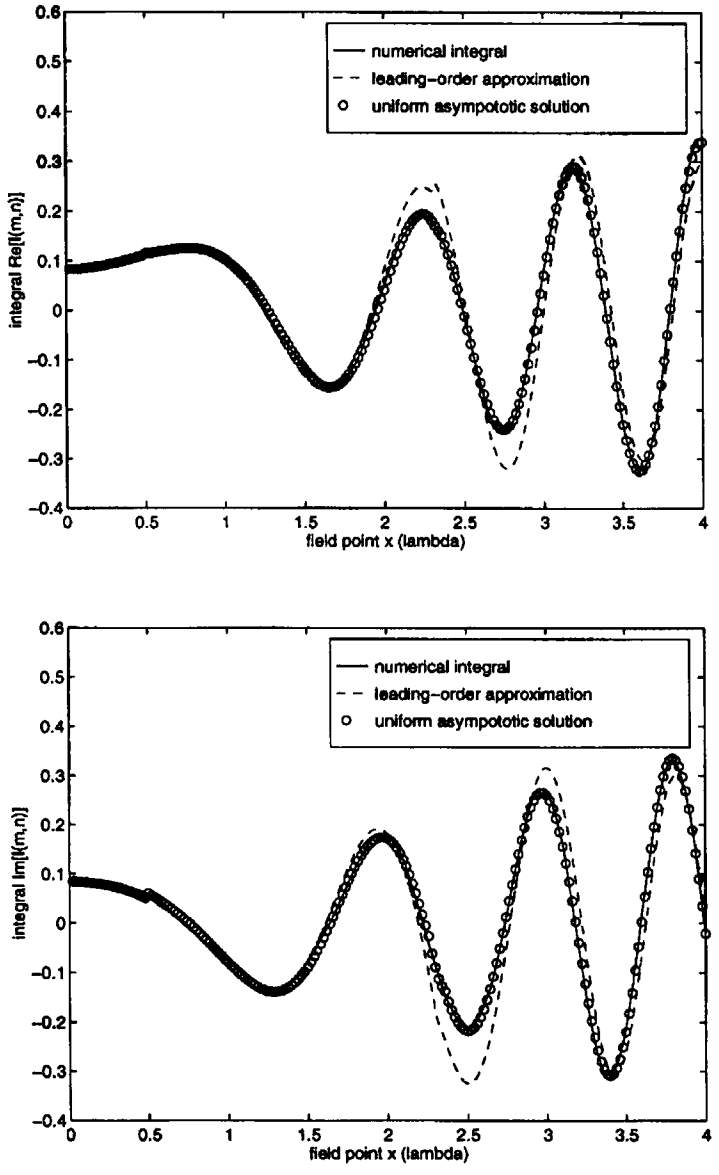

Figure 13. The computation results of integral $I(m,n)$ from the uniform asymptotic expansion method when $|z_m + z_n| = 4\lambda$. (a) Real part; (b) Imaginary part.

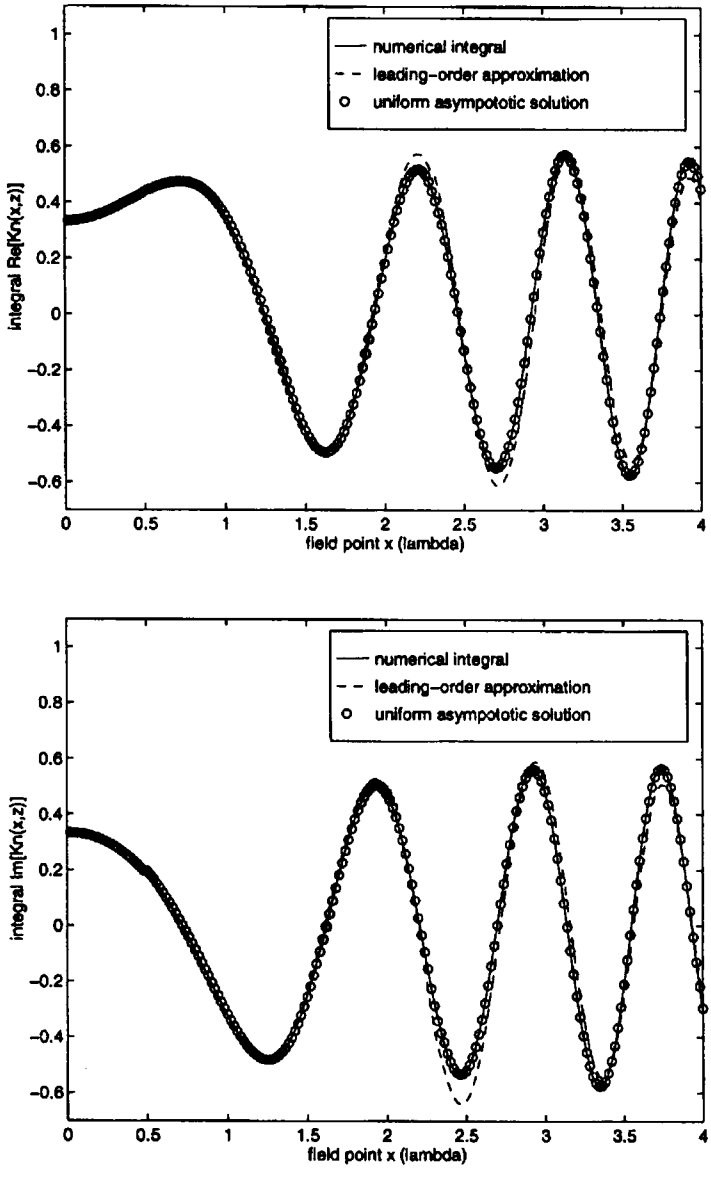

Figure 14. The computation results of integral $K_n(x, z)$ from the uniform asymptotic expansion method when $|z_n| = 4\lambda$. (a) Real part; (b) Imaginary part.

integral	$I(m,n)$		
method	numerical integral	leading-order approximation	uniform solution
CPU time(s)	18.9079	0.0070	0.0056
integral	$K_n(x,z)$		
method	numerical integral	leading-order approximation	uniform solution
CPU time(s)	4.5066	0.0023	0.0028

Table 2. The Comparison of CPU Time Used in the Computation of Integrals.

6. NUMERICAL EXAMPLES

In this section, we will use the fast evaluation methods described above to compute the scattering problem. The first example we considered is a buried dielectric square cylinder shown in Fig. 15(a). In our examples, we set $\epsilon_a = 1$ and $\epsilon_b = 4$. The TM wave is normally incident ($\theta' = 0$) with unit electric field. For the dielectric cylinder, the side length $d = 0.5\lambda$ and the relative permittivity $\epsilon_r = 20 + i15$. We use $N = 100$ cells to divide the square cylinder, which are numbered from the left to right and then from the bottom to top.

When the buried height $h = 0.5\lambda$ and $h = 2.5\lambda$, the internal electric fields inside the dielectric cylinder at each cell computed by the numerical-integral method and the fast-solution method are shown in Figs. 16 and 18, respectively. In these two cases, the scattered electric fields observed at $z = 0, 0.25\lambda$ and 0.5λ are illustrated in Figs. 17(a)-(c) and 19(a)-(c), respectively. From the computation results, we can clearly see that the internal electric fields from the fast evaluation method fit excellently those from the numerical integral, and the scattered electric fields from the fast evaluation method give a good approximation to those from the numerical integration. The reason why the internal fields are more accurate is because $I(m,n)$ is only an additional part in the matrix filling and the main part is accurate, as shown in (6) and (7). However, $K_n(x,z)$ is the sole contribution to the scattered fields. The fast evaluation method greatly reduces the computation time. The CPU time used in the two methods are illustrated in Tab. 3, in which the number of the observation points $M = 100$.

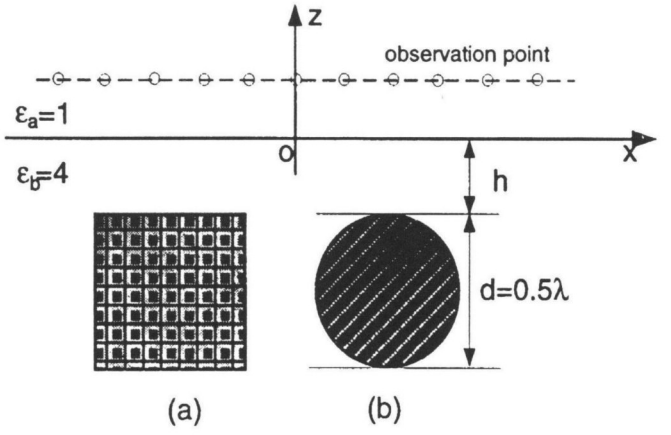

Figure 15. Examples: (a) A square dielectric cylinder and (b) A circular conducting cylinder buried under the half space.

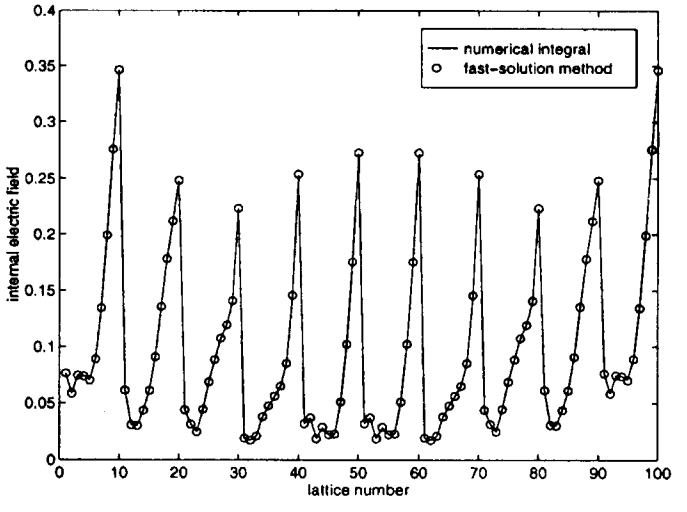

Figure 16. The internal electric fields inside the square dielectric cylinder when $h = 0.5\lambda$.

Next, we consider a circular conducting cylinder buried under the half space, as shown in Fig. 15(b). Here, the diameter of the circle is $d = 0.5\lambda$. We use $N = 100$ cells to divide the circular cylinder, which are numbered from the top point rotating to the right.

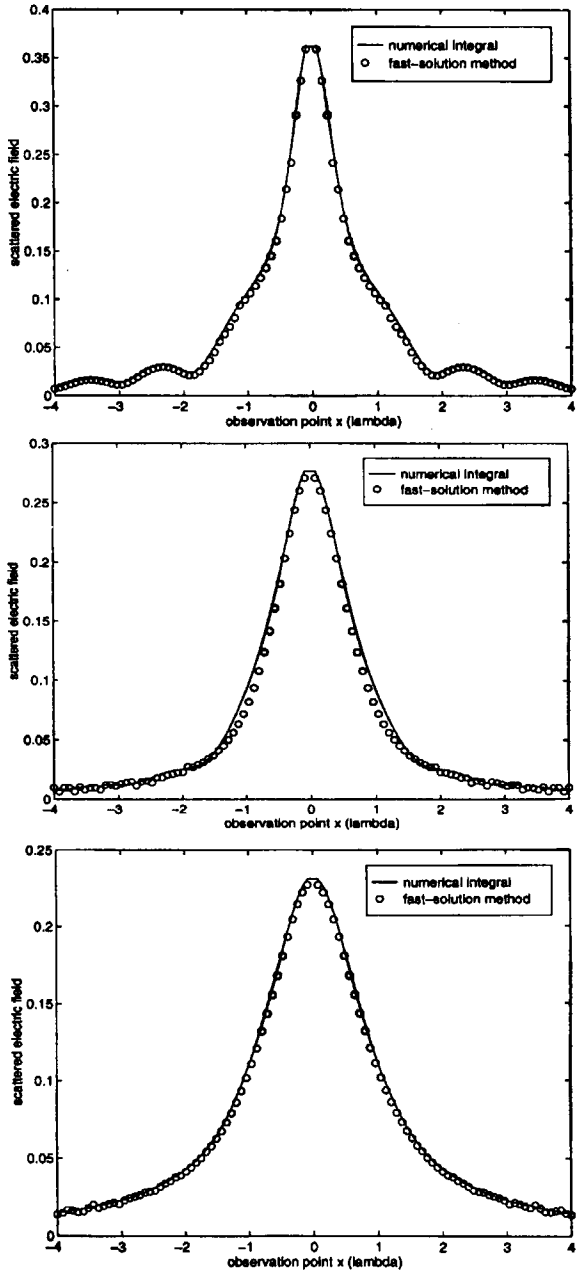

Figure 17. The scattered electric fields by the square dielectric cylinder when $h = 0.5\lambda$. (a) $z = 0$; (b) $z = 0.25\lambda$; (c) $z = 0.5\lambda$.

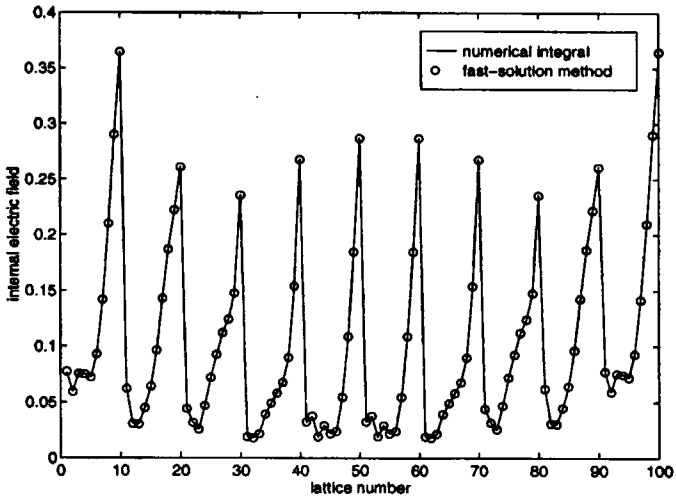

Figure 18. The internal electric fields inside the square dielectric cylinder when $h = 2.5\lambda$.

	matrix filling	matrix inversion	scattered field ($z = 0$)	scattered field ($z = 0.25\lambda$)	scattered field ($z = 0.5\lambda$)
numerical integral	597.68	0.17	155.40	436.20	959.38
fast evaluation	0.15	0.17	0.46	0.38	0.38

Table 3. The Comparison of CPU Time Used in the Scattering by Dielectric Cylinder.

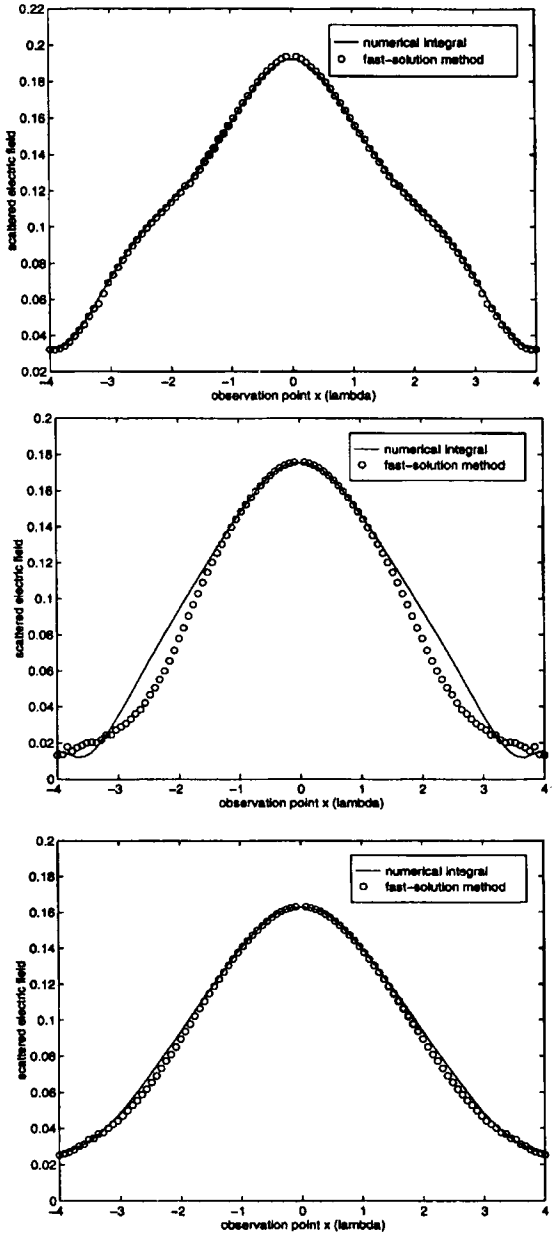

Figure 19. The scattered electric fields by the square dielectric cylinder when $h = 2.5\lambda$. (a) $z = 0$; (b) $z = 0.25\lambda$; (c) $z = 0.5\lambda$.

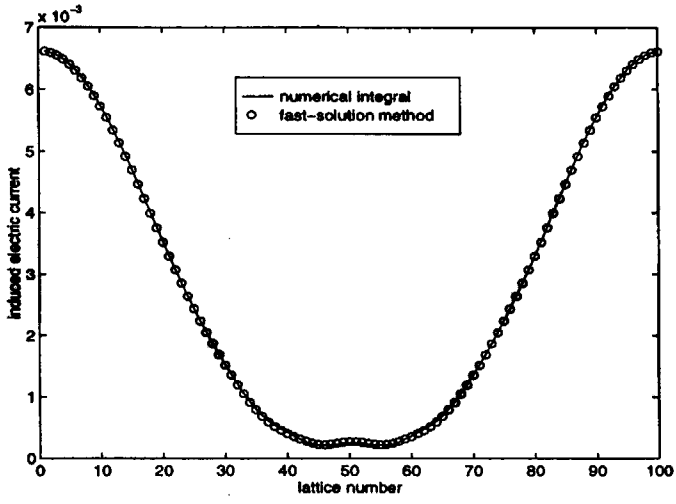

Figure 20. The induced electric currents around the circular conducting cylinder when $h = 0.5\lambda$.

Similar to the first example, when the buried height $h = 0.5\lambda$ and $h = 2.5\lambda$, the induced electric currents on the surface of the conducting cylinder from the both methods are shown in Figs. 20 and 22; the scattered electric fields at $z = 0, 0.25\lambda$ and 0.5λ are shown in Figs. 21(a)-(c) and 23(a)-(c), respectively. Again, the induced currents from the fast method are more accurate, and the scattered fields from the fast method give good approximations. The comparison of the CPU time for the buried conducting cylinder is illustrated in Tab. 4, in which the number of the observation points $M = 100$. From Tab. 4, the CPU time can be reduced over thousands of times by using the efficient matrix filling methods.

	matrix filling	matrix inversion	scattered field ($z = 0$)	scattered field ($z = 0.25\lambda$)	scattered field ($z = 0.5\lambda$)
numerical integral	308.71	0.17	142.72	471.58	1043.02
fast evaluation	0.16	0.17	0.48	0.38	0.38

Table 4. The Comparison of CPU Time Used in the Scattering by Conducting Cylinder.

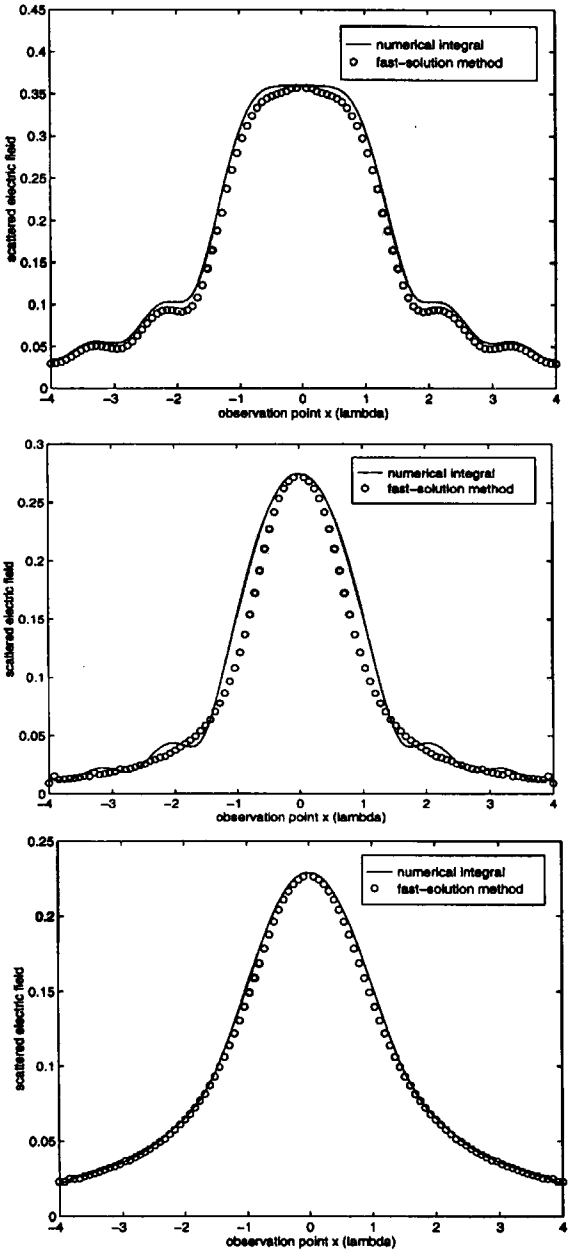

Figure 21. The scattered electric fields by the circular conducting cylinder when $h = 0.5\lambda$. (a) $z = 0$; (b) $z = 0.25\lambda$; (c) $z = 0.5\lambda$.

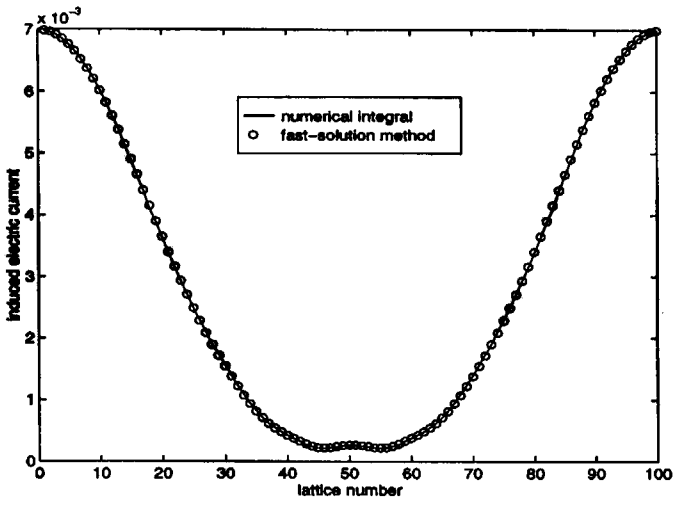

Figure 22. The induced electric currents around the circular conducting cylinder when $h = 2.5\lambda$.

We remark that the fast method to compute the internal electric fields (or surface electric currents) and scattered electric fields at $z = 0$ is the uniform asymptotic expansion method in the above examples, which gives accurate results. For the scattered fields at $z = 0.25\lambda$ and 0.5λ, we use the leading-order approximation of the steepest-descent method. From the numerical results, this approximation gives a good evaluation when $z \geq 0.5\lambda$. If z is smaller than 0.1λ, the uniform asymptotic method can be used.

In the above two examples, the buried scatterers are of small electrical size. Finally, we consider the scattering from a moderately conducting cylinder. See Fig. 15(b), when $d = 10\lambda$ and $h = 5\lambda$, the induced electric current on the surface of the conducting cylinder and the scattered electric fields at $z = 0$, λ and 2λ are shown in Figs. 24 and 25. Here the cell number $N = 500$, and the number of the observation point $M = 200$. Obviously, the fast method gives excellent evaluation to the moderately-sized buried problem, while the CPU time can be greatly saved, as shown in Tab. 5. Comparing Tab. 5 with Tab. 4, the fast method saves much more CPU time when N becomes larger.

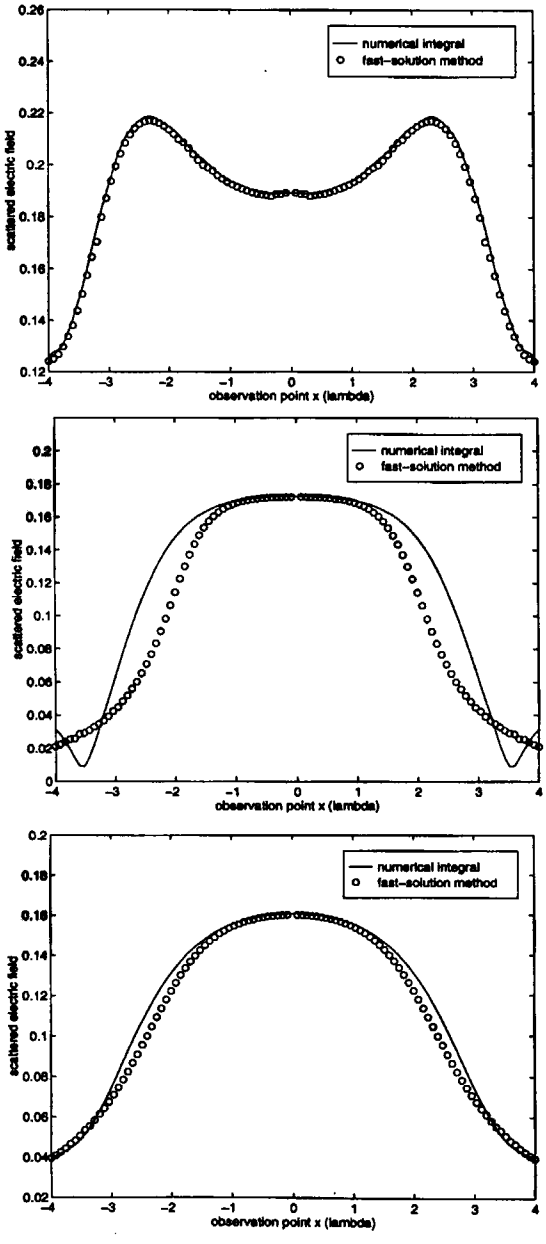

Figure 23. The scattered electric fields by the circular conducting cylinder when $h = 2.5\lambda$. (a) $z = 0$; (b) $z = 0.25\lambda$; (c) $z = 0.5\lambda$.

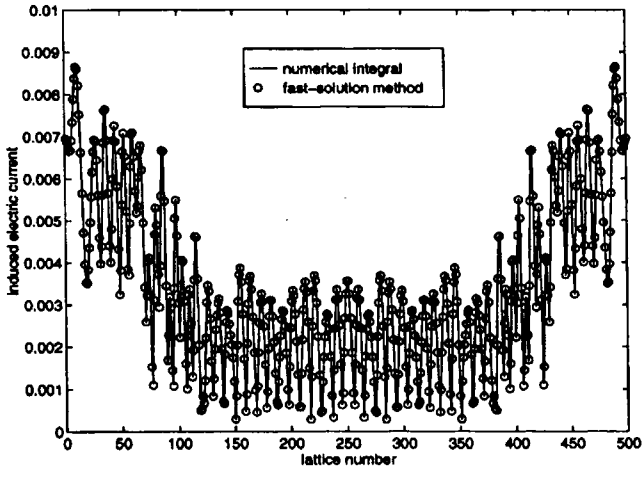

Figure 24. The induced electric currents around the circular conducting cylinder when $d = 10\lambda$ and $h = 5\lambda$.

	matrix filling	matrix inversion	scattered field ($z = 0$)	scattered field ($z = \lambda$)	scattered field ($z = 2\lambda$)
numerical integral	20325.79	5.27	1731.02	18896.40	42940.86
fast evaluation	4.14	5.27	1.98	2.46	2.48

Table 5. The Comparison of CPU Time Used in the Scattering by Moderately-Sized Conducting Cylinder.

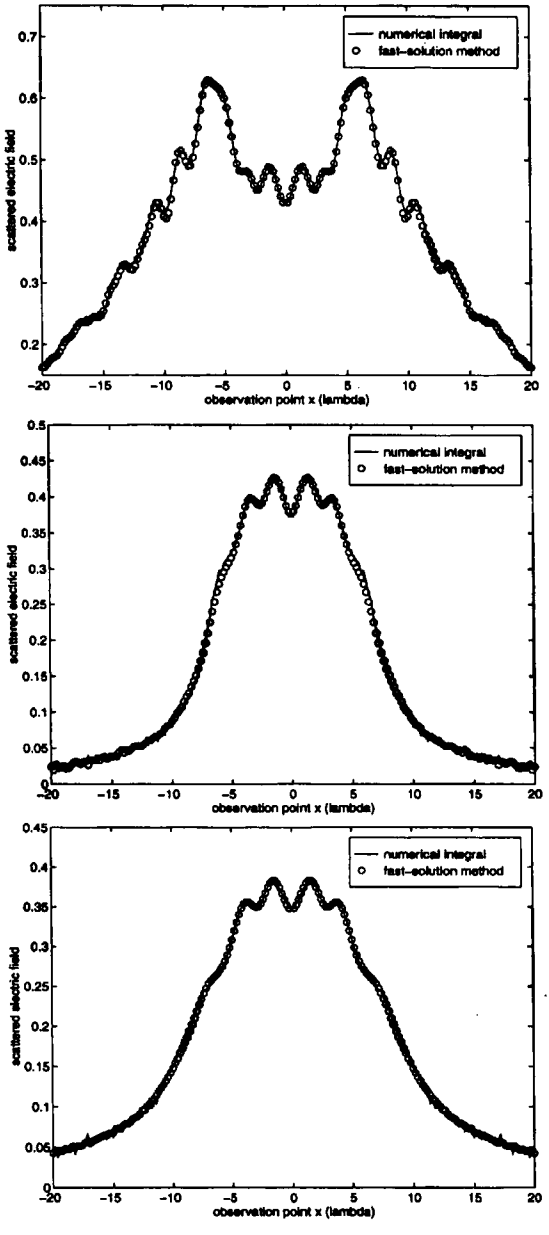

Figure 25. The scattered electric fields by the circular conducting cylinder when $d = 10\lambda$ and $h = 5\lambda$. (a) $z = 0$; (b) $z = \lambda$; (c) $z = 2\lambda$.

7. CONCLUSIONS

This paper has introduced several fast methods to treat two kinds of Sommerfeld integrals which appear in the TM wave scattering by two-dimensional buried cylinders. Analysis and numerical results show that the numerical-integral method along the steepest-descent path has a comparable precision to that along the original integrating path, but the CPU time can be reduced hundreds of times; the leading-order approximations of the steepest- descent method give good evaluation of the integrals except the near region of the critical angle, and the uniform asymptotic solutions can give good approximations in the whole region, but the CPU time will be reduced over thousands of times. Hence the buried scattering problem can be rapidly solved by using the fast evaluation methods, which makes it possible to handle larger buried scatterers. In addition, the fast computation of the forward scattering problem also makes it possible to investigate the inverse scattering by buried scatterers.

ACKNOWLEDGEMENTS

This work is supported by AFOSR under MURI grant F49620-96-1-0025, ONR under grant N00014-95-1-0872, and grant NSF ECS93-02145.

APPENDIX

From (76), we make $\theta_0 \to \theta_c$ from the side of $g_1 > 0$. Then we have

$$\lim_{\theta_0 \to \theta_c} \gamma_0 = \alpha_0 4\sqrt{k_a} \left(\lim_{t \to t_c} \frac{\sqrt{g_0}}{g_1} \right)^{\frac{3}{2}} = \alpha_0 4\sqrt{k_a} \left(\lim_{t \to t_c} \frac{g_0'}{2g_1'\sqrt{g_0}} \right)^{\frac{3}{2}}$$
$$= \alpha_0 4\sqrt{k_a} \left(\lim_{t \to t_c} \frac{\sqrt{2g_0''}}{2g_1'} \right)^{\frac{3}{2}} = \alpha_0 4\sqrt{k_a} \left(\frac{k_b^2 - k_a^2}{2k_b} \right)^{\frac{3}{4}}.$$

Here, the limit

$$\lim_{t \to t_c} \frac{g_0'}{\sqrt{g_0}} = \sqrt{2g_0''(t_c)}$$

has been used.

From (77), one obtains

$$\lim_{\theta_0\to\theta_c}\gamma_1 = \alpha_1 \lim_{t\to t_c} \frac{4\sqrt{k_a}\left[\left(\frac{\sqrt{g_0}}{g_1}\right)^{\frac{3}{2}}\right]' - \sqrt{2k_b}\left[\left(\frac{g_2}{\sqrt{g_0}}\right)^{\frac{1}{2}}\right]'}{\frac{g_0'}{2\sqrt{g_0}}}$$

$$= \frac{2\alpha_1}{\sqrt{2g_0''(t_c)}} \times \left\{4\sqrt{k_a}\lim_{t\to t_c}\left[\left(\frac{\sqrt{g_0}}{g_1}\right)^{\frac{3}{2}}\right]' - \sqrt{2k_b}\lim_{t\to t_c}\left[\left(\frac{g_2}{\sqrt{g_0}}\right)^{\frac{1}{2}}\right]'\right\}.$$

For the first limit, we have

$$\lim_{t\to t_c}\left[\left(\frac{\sqrt{g_0}}{g_1}\right)^{\frac{3}{2}}\right]' = \frac{3}{4}\lim_{t\to t_c}\left(\frac{\sqrt{g_0}}{g_1}\right)^{\frac{3}{2}}\lim_{t\to t_c}\frac{g_0'g_1 - 2g_0g_1'}{g_0g_1}$$

$$= \frac{3}{4}\left[\frac{\sqrt{2g_0''(t_c)}}{2g_1'(t_c)}\right]^{\frac{3}{2}}\frac{g_1'(t_c)g_0'''(t_c) - 3g_1''(t_c)g_0''(t_c)}{3g_1'(t_c)g_0''(t_c)} = 0$$

due to $g_1'(t_c)g_0'''(t_c) - 3g_1''(t_c)g_0''(t_c) = 0$.

For the second limit, we have

$$\lim_{t\to t_c}\left[\left(\frac{g_2}{\sqrt{g_0}}\right)^{\frac{1}{2}}\right]' = -\frac{1}{4}\lim_{t\to t_c}\left(\frac{g_2}{\sqrt{g_0}}\right)^{\frac{1}{2}}\lim_{t\to t_c}\frac{g_0'g_2 - 2g_0g_2'}{g_0g_2}$$

$$= -\frac{1}{4}\left[\frac{2g_2'(t_c)}{\sqrt{2g_0''(t_c)}}\right]^{\frac{1}{2}}\frac{g_2'(t_c)g_0'''(t_c) - 3g_2''(t_c)g_0''(t_c)}{3g_2'(t_c)g_0''(t_c)}$$

$$= \frac{k_b^2 - 6k_a^2}{2\sqrt{k_a\sqrt{2k_b(k_b^2 - k_a^2)}}}.$$

Hence, we obtain

$$\lim_{\theta_0\to\theta_c}\gamma_1 = \alpha_1\frac{6k_a^2 - k_b^2}{k_b\sqrt{k_a}}\left(\frac{k_b^2 - k_a^2}{2k_b}\right)^{\frac{1}{4}}.$$

REFERENCES

1. Harrington, R. F., *Field Computation by Moment Methods,* New York: Macmillan, 1968.
2. Richmond, J. H., "Scattering by a dielectric cylinder of arbitrary cross section," *IEEE Trans. Antennas Propagat.,* Vol. AP-13, 334–341, 1965.
3. Glisson, A. W. and D. R. Wilton, "Simple and efficient numerical methods for problems of electromagnetic radiation and scattering from surfaces," *IEEE Trans. Antennas Propagat.,* Vol. AP-28, 593–603, 1980.
4. Umashankar, K., A. Taflove and S. M. Rao, "Electromagnetic scattering by arbitrarily shaped three-dimensional homogeneous lossy dielectric objects," *IEEE Trans. Antennas Propagat.,* Vol. AP-34, 758–766, 1986.
5. Umashankar, K., and A. Taflove, "A novel method to analyze electromagnetic scattering of complex objects," *IEEE Trans. Electromagn. Compat.,* Vol. EMC-24, 397–405, 1982.
6. Yee, K. S., "Numerical solution of initial boundary value problems involving Maxwell's equations in isotropic media," *IEEE Trans. Antennas Propagat.,* Vol. AP-14, 302–307, May 1966.
7. Kunz, K. S., and R. J. Luebbers, *The Finite Difference Time Domain Method for Electromagnetics,* Boca Raton, FL: CRC, 1993.
8. Taflove, A., *Computational Electromagnetics: The Finite-Difference Time-Domain Method,* Boston, MA: Artech House, 1995.
9. Silvester, P. P., and R. L. Ferrari, *Finite Elements for Electrical Engineers,* second Ed., Cambridge, U. K.: Cambridge Univ. Press, 1990.
10. Jin, J. M., *The Finite Element Method in Electromagnetics,* New York: Wiley, 1993.
11. Chew, W. C., "Fast algorithms for wave scattering developed at the Electromagnetic Laboratory, University of Illinois," *IEEE Antennas Propagat. Mag.,* Vol. 35, 22–32, Aug. 1993.
12. Chew, W. C. et al., "Fast solution methods in Electromagnetics," *IEEE Trans. Antennas Propagat.,* Vol. AP-45, 533–543, Mar. 1997.
13. Rokhlin, V., "Rapid solution of integral equations of scattering theory in two dimensions," *J. Comput. Phys.,* Vol. 36, No. 2, 414–439, 1990.
14. Wagner, R. L., and W. C. Chew, "A study of wavelets for the solution of electromagnetic integral equations," *IEEE Trans. Antennas Propagat.,* Vol. AP-43, 802–810, Aug. 1995.
15. Steinberg, B. Z., and Y. Leviatan, "On the use of wavelet expansions in the method of moments," *IEEE Trans. Antennas Propagat.,* Vol. AP-41, 610–619, May 1993.
16. Han, G., and W. C. Chew, "A discrete BCG-FFT algorithm for solving 3-D inhomogeneous scatterer problem," *J. Electromagn. Waves Applicat.,* Vol. 9, No. 10 1339–1357, 1995.

17. Borup, D. T., and O. P. Gandhi, "Fast-Fourier transform method for calculation of SAR distributions in finely discritized inhomogeneous models of biological bodies," *IEEE Trans. Microwave Theory Tech.*, Vol. MTT-32, 355–360, Apr. 1984.
18. Song, J. M., and W. C. Chew, "Fast multipole method solution using parametric geometry," *Microwave Opt. Tech. Lett.*, Vol. 9, No. 16, 760–765, Nov. 1994.
19. Song, J. M., and W. C. Chew, "Multilevel fast-multipole algorithm for solving combined field integral equations of electromagnetic scattering," *Microwave Opt. Tech. Lett.*, Vol. 10, No. 1, 14–19, 1995.
20. Michielssen, E., and W. C. Chew, "Fast integral equation solver using plane-wave basis representation along the steepest descent path," in *URSI Radio Sci. Meet. Dig.*, 301, Newport Beach, CA, Jun. 1995.
21. Johnson, W. A., "Analysis of vertical, tubular cylinder which penetrates an air-dielectric interface and which is excited by an azimuthally symmetric source," *Radio Sci.*, Vol. 18, 1273–1281, 1983.
22. Burke, G. J., and E. K. Miller, "Modeling antennas near to and penetrating a lossy interface," *IEEE Trans. Antennas Propagat.*, Vol. AP-32, 1040–1049, 1984.
23. Karlsson, A., and G. Kristensson, "Electromagnetic scattering from subterranean obstacles in a stratified ground," *Radio Sci.*, Vol. 18, 345–356, 1983.
24. Butler, C. M., X. B. Xu and A. W. Glisson, "Current induced on a conducting cylinder located near the planar interface between two semi-infinite half-space," *IEEE Trans. Antennas Propagat.*, Vol. AP-33, 616–624, 1985.
25. Xu, X. B., and C. M. Butler, "Scattering of TM excitation by coupled and partially buried cylinders at the interface between two media," *IEEE Trans. Antennas Propagat.*, Vol. AP-35, 529–538, 1987.
26. Michalski, K. A., and D. Zheng, "Electromagnetic scattering and radiation by surfaces of arbitrary shape in layered media, Part I: Theory," *IEEE Trans. Antennas Propagat.*, Vol. AP-38, 335–344, 1990.
27. Michalski, K. A., and D. Zheng, "Electromagnetic scattering and radiation by surfaces of arbitrary shape in layered media, Part II: Implementation and results for contiguous half-spaces," *IEEE Trans. Antennas Propagat.*, Vol. AP-38, 345–352, 1990.
28. Cui, T. J., W. Wiesbeck and A. Herschlein, "Electromagnetic scattering by multiple dielectric and conducting objects buried under multilayered media, Part I: Theory," *IEEE Trans. Geoscience and Remote Sensing,* Vol. GE-35, (in press), 1997.
29. Cui, T. J., W. Wiesbeck and A. Herschlein, "Electromagnetic scattering by multiple dielectric and conducting objects buried under multilayered media, Part II: Numerical implementation and results," *IEEE Trans. Geoscience and Remote Sensing,* Vol. GE-35, (in press), 1997.

30. Cui, T. J., and W. Wiesbeck, "TM wave scattering by multiple two-dimensional scatterers buried under one-dimensional multi-layered media," *Proc. IEEE International Geoscience and Remote Sensing Symposium,* Vol. I, 763–765, Lincoln, 27–31 May, 1996.
31. Chew, W. C., *Waves and Fields in Inhomogeneous Media,* second Ed. New York: IEEE Press, 1995.
32. Bleistein, N., and R. A. Handelsman, *Asymptotic Expansions of Integrals.* New York: Holt, Rinehart and Winston, 1975.
33. Wait, J. R., *Electromagnetic Waves in Stratified Media.* London: Pergamon Press, 1962.
34. Lebedev, N. N., *Special Functions and Their Applications.* Englewood Cliffs, N.J.: Prentice-Hall, 1965.

Tie Jun Cui was born in September 1965, in Hebei, P R China. He received the B.Sc., M.Sc., and Ph.D. degrees in electrical engineering from Xidian University, Xi'an, P.R. China, in 1987, 1990, and 1993, respectively. In march 1993, he joined the Department of Microwave Telocommunications Engineering, Xidian University. He became an Associate Professor in Nov. 1993 at the same university. From 1995 to 1997 he was a Research Fellow with the Institut für Höchestfrequentztechnik und Elektronik (IHE) at the University of Karlsruche, Germany. In July 1997, he became a Post-doctoral Research Associate at the Center for Computational Electromagnetic, Department of Electrical and Computer Engineering in the University of Illinois at Urbana-Champaign. His research interests include electromagnetic scattering and inverse scattering, wave propagation, and numerical methods. Dr. Cui was awarded a Research Fellowship from the Alexander von Humboldt Foundation, Bonn, Germany, in 1995. He is a senior member of the China Institute of Electronics (CIE).

Weng Cho Chew was born on June 9, 1953 in Malaysia. He received the B.S. degree in 1976, both the M.S. and Engineer's degrees in 1978, and the Ph.D. degree in 1980, all in electrical engineering from the Massachusetts Institute of Technology, Cambridge. His recent research interest has been in the area of wave propagation, scattering, inverse scattering, and fast algorithms related to scattering, inhomogeneous media for geophysical subsurface sensing and nondestructive testing applications. Previously, he has also analyzed electrochemical effects and dielectric properties of composite materials, microwave and optical waveguides, and microstrip antennas. From 1981 to 1985, he was with Schlumberger-Doll Research in Ridgefield, Connecticut, where he was a program leader and later a department manager. From 1985 to 1990, he was an associate professor with the University of Illinois. He currently is a professor there and teaches graduate courses in Wave and Fields in Inhomogeneous Media, and Theory of Microwave and Optical Waveguides and supervises a graduate research program. His name is listed many times in the List of Excellent Instructors on campus. He has authored

a book Waves and Fields in Inhomogeneous Media, published over 175 scientific journal articles and presented over 200 conference papers. Dr. Chew is a member of Eta Kappa Nu, Tau Beta Pi, URSI Commissions B and F, and an active member with the Society of Exploration Geophysics. He is an IEEE Fellow and was an NSF Presidential Young Investigator for 1986. He was also an AdCom member IEEE Geoscience and Remote Sensing Society, and is presently an associate editor of the *IEEE Transactions of Geoscience and Remote Sensing, Journal of Electromagnetic Waves and Applications,* and *Microwave Optical Technology Letters.* He was also an associate editor with the *International Journal of Imaging Systems and Technology,* and has been a Guest Editor of *Radio Science, International Journal of Imaging Systems and Technology and Electromagnetics.* From 1989 to 1993, he was the associate director the Advanced Construction Technology Center at the University of Illinois. Presently, he is the director of the Center for Computational Electromagnetics and the Electromagnetics Laboratory at the same university.